Atmospheric
Chemistry
and Physics

Effect of wind speed on marine aerosol optical properties over remote oceans with use of spaceborne lidar observations

Kangwen Sun[1], **Guangyao Dai**[1], **Songhua Wu**[1,2,3], **Oliver Reitebuch**[4], **Holger Baars**[5], **Jiqiao Liu**[6], and **Suping Zhang**[7]

[1]College of Marine Technology, Faculty of Information Science and Engineering,
Ocean University of China, 266100 Qingdao, China
[2]Laoshan Laboratory, 266237 Qingdao, China
[3]Institute for Advanced Ocean Study, Ocean University of China, 266100 Qingdao, China
[4]Institut für Physik der Atmosphäre, Deutsches Zentrum für Luft- und Raumfahrt e.V. (DLR),
82234 Oberpfaffenhofen, Germany
[5]Leibniz Institute for Tropospheric Research (TROPOS), 04318 Leipzig, Germany
[6]Laboratory of Space Laser Engineering, Shanghai Institute of Optics and Fine Mechanics,
Chinese Academy of Sciences, 201800 Shanghai, China
[7]Physical Oceanography Laboratory, Ocean University of China, 266100 Qingdao, China

Correspondence: Guangyao Dai (daiguangyao@ouc.edu.cn)

Abstract. Marine aerosol affects the global energy budget and regional weather. The production of marine aerosol is primarily driven by wind at the sea–air interface. Previous studies have explored the effects of wind on marine aerosol, mostly by examining the relationships between aerosol optical depth (AOD) and surface wind speed. In this paper, utilizing the synergy of aerosol and wind observations from Aeolus, the relationships between the marine aerosol optical properties at 355 nm and the instantaneous co-located wind speeds of remote oceans are investigated at two vertical layers (within and above the marine atmospheric boundary layer (MABL)). The results show that the enhancements of the extinction and backscatter coefficients caused by wind are larger within the MABL than above it. The correlation models between extinction and backscatter with wind speed were established using power-law functions. The slope variation points occur during extinction and backscatter coefficients increasing with wind speed, indicating that the wind-driven enhancement of marine aerosol involves two phases: a rapid-growth phase with high wind dependence, followed by a slower-growth phase after the slope variation points. We also compared the AOD–wind relationship acquired from Aeolus with CALIPSO-derived results from previous research. The variation in the lidar ratio with wind speed is examined, suggesting a possible "increasing–decreasing–increasing" trend of marine aerosol particle size as wind speed increases. This study enhances the comprehension of the correlation between marine aerosol optical properties and wind speed by providing vertical information and demonstrating that their relationships are more complex than a linear or exponential relation.

1 Introduction

According to the Intergovernmental Panel on Climate Change (IPCC) Fifth Assessment Report, the total emission of marine aerosol (including marine primary organic aerosol) produced from oceans is 1400–6800 Tg yr^{-1}, which is considered the largest natural aerosol input to the atmosphere globally (Boucher et al., 2013). Accurate estimations of marine aerosol production, evolution, and dissipation, as well as the knowledge of marine aerosol spatial and temporal distribution, are significant for studying the global energy budget, aerosol–cloud interactions and visibility changes (Latham and Smith, 1990; Murphy et al., 1998; O'Dowd et al., 1999; Haywood et al., 1999; de Leeuw et al., 2000; Kaufman et al., 2002; Smirnov et al., 2012). Radiative forcing caused by marine aerosol is a significant contributor to the global energy budget. It was reported that the average marine aerosol optical depth (AOD_{mar}) is approximately 0.15, while the volume concentration of cloud condensation nuclei from marine aerosol is around 60 cm^{-3} (Kaufman et al., 2002; Lewis and Schwartz, 2004). Therefore, marine aerosol has both direct and indirect impacts on radiative forcing by scattering and absorbing solar radiation and by modifying the microphysical properties of clouds, respectively (Murphy et al., 1998; Pierce and Adams, 2006). Knowledge of the impact of the magnitude of, and changes in, marine aerosol emissions on the shifts in climate and marine ecosystem processes is limited (IPCC, 2021).

Marine aerosol mainly includes primary sea spray particles and secondary aerosols produced by the oxidation of emitted precursors. Sea spray particles, composed of sea salt and primary organic aerosols, are produced by wind-induced wave breaking and the wind-driving direct mechanical disruption of wave crests (O'Dowd and de Leeuw, 2007; IPCC, 2021). Moreover, as a dynamical meteorological factor, wind speed also has vital influence on the transport, evolution, and dissipation of aerosols. Consequently, wind speed is a crucial factor which governs the production and life cycle of marine aerosol (Lewis and Schwartz, 2004). Exploring accurately the relationships between marine aerosol optical properties (aerosol optical depth (AOD), extinction coefficient (α), backscatter coefficient (β), etc.) and wind speed is significant for improving global aerosol transport models (Jaeglé et al., 2011; Madry et al., 2011; Fan and Toon, 2011), for enhancing satellite-retrieved AODs (Kahn et al., 2010; Kleidman et al., 2012), for atmospheric correction of ocean color (Zibordi et al., 2011), and for the study of biogeochemical cycles (Meskhidze and Nenes, 2010). Several efforts have been reported to investigate the relationship between the AOD or aerosol extinction coefficient over the ocean and wind speed. Utilizing either satellite-retrieved AODs (Glantz et al., 2009; Huang et al., 2010; Lehahn et al., 2010; O'Dowd et al., 2010; Grandey et al., 2011) or surface (coast, island, or ship)-based measurement AODs (Platt and Patterson, 1986; Villevalde et al., 1994; Smirnov et al., 1995;

Wilson and Forgan, 2002; Smirnov et al., 2003; Shinozuka et al., 2004; Mulcahy et al., 2008; Lehahn et al., 2010; Adames et al., 2011; Sayer et al., 2012; Smirnov et al., 2012), most previous research focused on the AOD measured by passive instruments (mainly sun photometers). From these studies, various power-law or linear relationships have been established showing a positive correlation between AODs over the ocean and surface wind speed. However, passive instruments lack the ability to distinguish marine aerosol from other aerosols, to obtain vertical profiles of aerosols, and to retrieve aerosol optical properties in the absence of sunlight (except for lunar photometers) and under cloudy conditions (Kiliyanpilakkil and Meskhidze, 2011; Winker and Pelon, 2003). Active optical instruments for aerosol measurements, mainly lidar, were also used to reveal the relationship between AOD or the extinction coefficient of marine aerosol and wind speed. A shipborne depolarization lidar was occupied to acquire aerosol extinction coefficients over the East Sea of Korea near Busan and Pohang, associated with the wind measurement from an anemometer mounted on a mast, finding a positive linear relationship ($R^2 = 0.57$) between extinction (532 nm) at 300 ± 50 m and wind speed at 20 m (Shin et al., 2014). However, this relationship was established using offshore data, and thus it can not be representative of the global ocean. The Cloud-Aerosol Lidar with Orthogonal Polarization (CALIOP) onboard the Cloud-Aerosol Lidar and Infrared Pathfinder Satellite Observation (CALIPSO) mission is capable of measuring the vertical distributions of global aerosol optical properties and identifying different aerosol types (including "clean marine"). Kiliyanpilakkil and Meskhidze (2011) selected CALIOP-retrieved pure AOD_{mar} below 2 km over the ocean utilizing the CALIOP aerosol subtype products and combined them with the surface wind speed provided by the Advanced Microwave Scanning Radiometer (AMSR-E) on board the Aqua satellite, acquiring a relatively complex increasing regression function, which will be presented and compared in Sect. 4.4.2. Furthermore, Prijith et al. (2014) also made use of CALIOP-retrieved AODs below 0.5 km over the ocean and the surface wind speed, obtaining nearly positive correlation linear relationships. Nevertheless, the assumed marine aerosol lidar ratio (LR_{mar}) (20 sr at 532 nm) was used in the AOD_{mar} retrieval process of CALIOP (Kiliyanpilakkil and Meskhidze, 2011), but the LR_{mar} can vary from 10 sr to around 40 sr at 532 nm (Groß et al., 2013, 2015; Bohlmann et al., 2018; Floutsi et al., 2023), which could generate deviations in the retrieval of AOD_{mar}. In summary, to explore accurately the relationship between marine aerosol optical properties and wind speed, it is essential to conduct global continuous observations and obtain the information of aerosol type identification, while vertical profiles of aerosols can provide extra spatial information for further analysis. Moreover, previous studies mostly focused on layer AOD_{mar} and ocean surface wind speed to explore the probable production of marine aerosol driven by surface wind. The relationship between the vertical optical proper-

ties of marine aerosol and the corresponding spatiotemporally synchronous wind speed, which represents the marine-atmospheric background state and may reveal the transport and evolution of marine aerosol vertically, remains to be investigated.

The Atmospheric Laser Doppler Instrument (ALADIN), the first-ever spaceborne direct detection wind lidar, which was launched into space in August 2018, was the unique payload installed on the Aeolus satellite mission of the European Space Agency (ESA) (Stoffelen et al., 2005; Reitebuch, 2012; Kanitz et al., 2019). As a direct detection high-spectral-resolution lidar, ALADIN was capable of providing the global aerosol optical property (e.g., α and β) profiles at 355 nm (Level-2A product), the horizontal-line-of-sight (HLOS) wind speed profiles (Level-2B product), and the wind vector profile from the European Centre for Medium-Range Weather Forecasts (ECMWF) model along the Aeolus track (Level-2C product) (Rennie et al., 2020). It should be emphasized that the aerosol and wind products are retrieved from the backscattered signal of the same laser light pulse emitted by ALADIN into the atmosphere, and hence the geolocation and time information of these products is completely consistent for each profile. The maximum detection height of these products is around 20 km and the vertical resolutions vary from 0.25 to 2 km (from bottom to top). Though regarded as a by-product, the particle optical property products have been demonstrated to provide valuable information about particles, especially on the detection and characterization of aerosol and cloud layers as well as on the lidar ratios (LRs) (Baars et al., 2021; Flament et al., 2021; Abril-Gago et al., 2022). Dai et al. (2022) conducted the first attempt on the combined application of the aerosol products (Level-2A products) and the wind vector products (Level-2C products) of ALADIN, observing an enormous dust transport event from the Sahara to the Americas in June 2020 and describing the transport quantitatively by calculating dust advection.

As mentioned above, Aeolus can provide global aerosol optical property profiles and wind speed profiles with high spatial and temporal resolution. Additionally, CALIOP can provide global aerosol type information. Hence, the combination of Aeolus–CALIOP products is capable of analyzing the relationship between marine aerosol optical properties (e.g., α, β, and LR) at 355 nm and wind speed globally and vertically. In this paper, utilizing the Aeolus Level-2A and Level-2C products together with the CALIOP aerosol subtype products, we (1) select ocean areas far from land and examine the dominance of marine aerosol over these areas using the CALIOP aerosol classification products; (2) attempt to acquire the pure marine aerosol optical properties (α, β, and LR) at 355 nm and the corresponding wind speeds from the Aeolus products, and to analyze the spatial distributions of these atmospheric state parameters at two separate vertical layers (0–1 km and 1–2 km, corresponding to the layers within and above the marine atmospheric boundary layer

(MABL), respectively); and (3) investigate the relationship between the marine aerosol optical properties and the wind speeds vertically over the ocean. Generally, the highlights of this work mainly include (1) determining the spatiotemporally synchronous relationship between aerosol optical properties (α, β, and LR) and instantaneous wind speeds, which could indicate the background atmospheric states within and above the MABL over remote oceans, and (2) performing the analysis at two separate height layers above the ocean surface to explore the vertical differences in wind-driven marine aerosol evolution.

This paper is organized as follows: Sect. 2 introduces the spaceborne lidars and their specific products used in this study. Section 3 presents the methodology of study area selection, data pre-processing, and data analyses for relationship exploration between marine aerosol optical properties and wind speed. Section 4 presents the procedure of study area selection, then analyses and discusses marine aerosol optical properties, wind speed, and their relationship above three selected areas.

2 Spaceborne lidars and products

2.1 ALADIN

Since its launch in August 2018, ALADIN globally observed the profiles of the components of the wind vector along the laser's line of sight (LOS), and also the profiles of aerosol optical properties, for more than 4 years. Aeolus flew at a mean altitude of about 320 km in a sun-synchronous orbit with local Equator crossing times of about 06:00 and 18:00 LT, a daily quasi-global coverage (about 16 orbits per day), and an orbit repeat cycle of 1 week (111 orbits) (Reitebuch, 2012). Designed as a high-spectral-resolution lidar with a laser wavelength of 354.8 nm, ALADIN has the capability to simultaneously acquire wind profiles and particle optical properties with its two separate optical frequency discrimination channels named Rayleigh channel and Mie channel. Detailed descriptions of the instrument design and the measurement concept are introduced in, for example, Ansmann et al. (2007), Dabas et al. (2008), Flamant et al. (2008), Reitebuch (2012), Lux et al. (2020), and Flament et al. (2021).

Processed in different phases, the Aeolus data products are classified into several levels: Level 0 (instrument housekeeping data), Level 1B (engineering-corrected HLOS winds), Level 2A (aerosol and cloud layer optical properties), Level 2B (meteorologically representative HLOS winds) and Level 2C (Aeolus-assisted wind vectors) (Flamant et al., 2008; Tan et al., 2008; Rennie et al., 2020). It should be emphasized that Level-2C wind vectors are the output from the assimilation of the Aeolus Level-2B products in the ECMWF operational numerical weather prediction (NWP) model after 9 January 2020 (Rennie et al., 2021). In addition, the products of Aeolus are available in different baselines which correspond to different processor versions used to derive the

products. The products were initially released as Baseline 07 and have been updated to Baseline 14 up to the time of this study (https://aeolus-ds.eo.esa.int/oads/access/; last access: 16 February 2023). As mentioned above, we use Level-2A and Level-2C products to study the relationship between marine aerosol optical properties and wind speed. Because Level-2C products can provide both components of the wind vector, we use Level-2C instead of Level-2B products from Aeolus. The time coverage of the Aeolus products used in this study is from 20 April 2020 to 4 July 2022. Thus, in terms of the Level-2A products used, the data processors are Baseline 11 (20 April 2020 to 26 May 2021), Baseline 12 (26 May 2021 to 6 December 2021), Baseline 13 (6 December 2021 to 29 March 2022), and Baseline 14 (29 March 2022 to 4 July 2022), while in terms of the Level-2C products, the data processors are Baseline 09 (20 April 2020 to 9 July 2020), Baseline 10 (9 July 2020 to 8 October 2020), Baseline 11 (8 October 2020 to 26 May 2021), Baseline 12 (26 May 2021 to 6 December 2021), Baseline 13 (6 December 2021 to 29 March 2022), and Baseline 14 (29 March 2022 to 4 July 2022), respectively (https://aeolus-ds.eo.esa.int/oads/access/; last access: 16 February 2023). The Level-2C NWP wind vector products from ECMWF used in this study are obtained after assimilation of the Level-2B observed HLOS wind products.

2.2　CALIOP

CALIOP, one of the payloads installed on CALIPSO, measured global vertical profiles of aerosol and cloud optical properties for more than 16 years starting in 2006. It can provide α at 532 and 1064 nm, β at 532 and 1064 nm, the depolarization ratio at 532 nm, vertical feature mask (VFM) products, and more. (Winker et al., 2009). The VFM products comprise the vertical information along each profile for cloud and aerosol identification, and further for the subtype classification of clouds and aerosols. For cloud and aerosol identification, the cloud–aerosol discrimination (CAD) algorithm was applied based on the layer-integrated volume depolarization ratio, layer-integrated total attenuated color ratio, and layer-averaged attenuated backscatter at 532 nm, as well as latitude and altitude (Liu et al., 2019). Aerosol subtypes are distinguished as "marine", "dusty marine", "dust", "polluted dust", "continental", "polluted continental", "elevated smoke", and "others" via the joint analysis of the particulate depolarization ratio, integrated attenuated backscatter coefficient at 532 nm, layer top altitude, layer base altitude, and surface type (Kim et al., 2018). In this study, CALIOP Level (L2) VFM products are applied to confirm the dominance of the marine aerosol over the selected ocean areas. Different versions of the CALIOP L2 VFM product are used, namely 4.10 (20 April 2020 to 1 July 2020), 4.20 (1 July 2020 to 19 January 2022), and 3.41 (19 January 2022 to 4 July 2022).
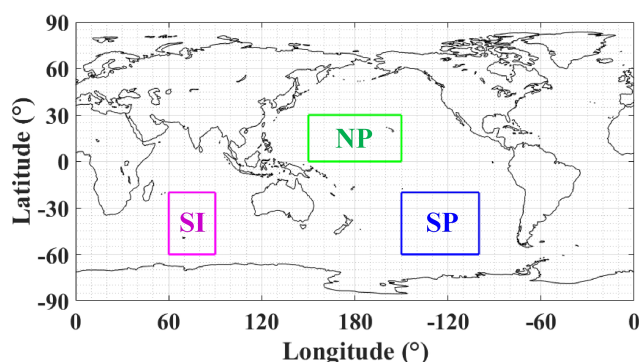

Figure 1. The selected ocean study areas.

3　Methodology

In general, the data processing and analysis procedure of this study can be summarized briefly in three parts, including the selection of the study areas, data pre-processing, and data analyses.

This work mainly focuses on marine aerosol, and hence the ocean areas for the study are supposed to be far away from land to reduce the influence of terrestrial aerosols, e.g., anthropogenic activities, dust, and biomass burning. In this work, we selected three ocean areas located in the North Pacific (NP), South Pacific (SP), and South Indian (SI) oceans, with the latitude and longitude ranges of 0–30° N and 150° E–150° W , 20–60° S and 100–150° W, as well as 20–60° S and 60–90° E, respectively, as shown in Fig. 1. Therefore, in this paper, we refer to these three remote ocean areas as "the NP area", "the SP area", and "the SI area", respectively.

The aerosol classification information from the CALIOP VFM products is utilized to statistically analyze the aerosol types of the selected areas. It is found that marine aerosol is mostly distributed in the altitude range of 0–2 km during VFM processing. Therefore, the statistical analysis of the aerosol types is conducted in the same altitude range. Marine aerosol is considered to dominate in the selected area if the percentage of the aerosol subtype "marine" is larger than 75 % while the percentage sum of "marine" and "dusty marine" is above 90 %; if so, then the study can be continued for this area.

The α at 355 nm and β at 355 nm retrieved by the standard correction algorithm (SCA) from the Aeolus Level-2A product are used in this study, as the SCA processing is capable of producing more stable α and β than the Mie channel algorithm (Flament et al., 2021). Furthermore, the mid-bin product (sca_optical_properties_mid_bins) of the SCA product is chosen because the mid-bin algorithm is more robust (Baars et al., 2021; Flament et al., 2021). To ensure high data quality for the study of the relationship between the optical properties and wind speed, a rigorous quality control has to be applied. In the aspect of quality control, negative α and β are

excluded, and then the quality flags ("bin_1_clear" and "processing_qc_flag") provided in the Level-2A product are applied to filter out invalid data (Trapon et al., 2022). Additionally, the outliers are labeled and eliminated by the boxplot analysis. Using the lower quartiles Q_L (25 % positions of the data) and the upper quartiles Q_U (75 % positions of the data), this method classifies the data below $Q_L - 3 \cdot (Q_U - Q_L)$ or above $Q_L + 3 \cdot (Q_U - Q_L)$ as outliers (Hoaglin et al., 1986). The Aeolus products do not differentiate between aerosol and cloud, which means that the particle optical properties of a single data bin may contain a mixture of both types of information. Aeolus-measured particulate β, combined with relative humidity (RH) and molecular β from the ECMWF NWP model provided in the Level-2A product, is utilized to screen the cloud layers. A cloud is considered quite likely to be present if the backscatter ratio (BR) (total backscatter coefficient divided by molecular backscatter coefficient) at 355 nm is larger than 2.5 or the RH is larger than 94 % (Flamant et al., 2020). Therefore, in this study, if the BR is larger than 2.5 or the RH is higher than 94 %, the corresponding data bin is considered to be cloud contaminated and is eliminated. With this cloud screening approach, in this study, 9 %, 35 %, and 40 % of the data in the altitude range of 0–2 km were eliminated for the NP area, the SP area, and the SI area, respectively. Due to the instrument design of ALADIN, it can only detect the co-polar backscattered light, leading to the lack of the depolarized portion of the β (Flamant et al., 2020). According to Groß et al. (2015), the depolarization ratio at 355 nm of marine aerosol ($\delta_{mar,355\,nm}$) is approximately 0.02 when the RH is larger than 50 %. Nevertheless, dried marine aerosol layers can significantly depolarize with the depolarization ratios varying from 0.02 to around 0.1, making the typical $\delta_{mar,355\,nm}$ of humid marine aerosol (RH > 50 %) unsuitable for dried aerosol (Haarig et al., 2017; Bohlmann et al., 2018). Consequently, to correct the marine aerosol backscatter coefficient with the typical $\delta_{mar,355\,nm}$ of humid marine aerosol, the data with RH > 50 % are retained (around 95 % of the data are retained), and thus with the typical $\delta_{mar,355\,nm}$ the total marine aerosol backscatter coefficient β_{mar} can be calculated by Eq. (1):

$$\beta_{mar} = (1 + \delta_{mar,355\,nm}) \cdot \beta_{mar,Aeolus\text{-}co}, \qquad (1)$$

where $\beta_{mar,Aeolus\text{-}co}$ is the original marine aerosol backscatter coefficient measured by ALADIN. It should be noted that all the aerosol β values from Aeolus identified as $\beta_{mar,Aeolus\text{-}co}$ values and then utilized to calculate β_{mar} values by Eq. (1) are under the ideal assumption that marine aerosol is the only aerosol type in the study areas. Though the study areas are all located in remote oceans far away from land and are evaluated as "marine aerosol dominates" by CALIOP, there are a few terrestrial aerosols like dust, polluted dust, polluted continental, and smoke, with a total proportion of no more than 10 % (see Sect. 4.1 for details). For terrestrial aerosols, the depolarization ratios at 355 nm are 0.22–0.24 for dust, 0.16 for polluted dust, 0.01 for polluted continental, and 0.03 for

smoke, among which those for dust and polluted dust are much larger than $\delta_{mar,355\,nm}$ (Floutsi et al., 2023). Consequently, regarding all the aerosols as marine aerosol and correcting β_{mar} according to Eq. (1) leads to an obvious underestimation in the β for dust and polluted dust. Nevertheless, in view of the small proportions of dust (maximum 3.15 %) and polluted dust (maximum 0.79 %) above the study areas, and thanks to the statistical analyses of the data for a long period, the assumption that all aerosols are considered as marine aerosol does not critically impact the β_{mar}–wind speed relationship, although it should be noted that the actual β is a little bit larger than the β_{mar}.

As for the wind vector data, the Aeolus Level-2C product provides the u component (zonal components of the wind vector) and the v component (meridional components of the wind vector) from the ECMWF model after assimilation of the Level-2B observational wind product, in the same data bins of the Level-2A optical properties product. Hence, the wind speed (ws) can be calculated with these two components by Eq. (2):

$$ws = \sqrt{u^2 + v^2}. \qquad (2)$$

With the reprocessed marine aerosol optical properties extinction coefficient α_{mar} and β_{mar}, and the corresponding wind speed, it is possible to explore the relationship between these parameters. At the beginning of the data analyses, α_{mar}, β_{mar}, and wind speed within the altitude range of 0–2 km are selected, where marine aerosol dominates according to the analysis of CALIOP VFM. Furthermore, the whole study height range is divided into two individual layers. Referring to the results of Luo et al. (2014, 2016) and Alexander and Protat (2019), the MABL height of remote oceans is summarized to be around 1 km. Moreover, calculated with ECMWF-provided boundary layer heights at the three study areas for the time period of 20 April 2020 to 26 May 2021, the mean values and the standard deviations are 787.47 ± 231.77 m at the NP area, 939.39 ± 360.20 m at the SP area, and 1005.29 ± 366.60 m at the SI area. Hence, the boundary height of the two vertical layers is set at 1 km, which is approximately the mean MABL height of remote oceans. Though the MABL heights are variable and therefore setting 1 km will lead to potential inaccuracies, the relatively low height resolution of Aeolus (0.25 km below 0.5 km, 0.5 km in the altitude of 0.5–2 km) limits the use of more precise height boundaries. The statistical results of the 0–1 km layers and the 1–2 km layers are considered generally representative of the atmospheric conditions within the MABL and above the MABL. In this paper, the lower layer with the altitude range of 0–1 km is called Layer$_L$ and the higher layer with the altitude range of 1–2 km is called Layer$_H$. It is important to note that the lowest altitude bins of Aeolus observation products may contain the reflections from the surface or even be subsurface, and thus they are contaminated and not representative of the atmospheric wind

speed and the aerosol optical properties (Wu et al., 2022). Regarding the ocean applications of spaceborne lidar observations, it is known that the lidar attenuated backscatter coefficients of the bin containing the ocean surface can be affected by the processes at the surface of the ocean, namely, stronger winds resulting in weaker backscattering (Josset et al., 2008). Labzovskii et al. (2023) indicated that Aeolus return signals are unlikely sensitive to ocean surface dynamical conditions (related to wind), which makes the analysis of marine aerosol optical properties in the MABL free from adverse effects stemming from the ocean surface. Nevertheless, during the data processing, it was discovered that all data (Level-2A particle optical properties and Level-2C wind vectors) below 0.25 km, which could be contaminated by reflections from the land or ocean surface, were screened out using Aeolus quality control flags, and then the lowest data bins were at around 0.25 km. This may indicate that the actual altitude range of marine aerosol optical properties in $\mathrm{Layer_L}$ is around 0.25–1 km. Although the data near the sea–air interface are missing, all available data avoid the contamination of the ground return signals and eliminate the risk of being affected by ocean surface dynamical conditions. Over the selected ocean areas, the spatial distributions of the α_{mar}, β_{mar}, and wind speed are acquired with the longitude–latitude grid of $5° \times 5°$ at two separate layers. Then the relationship analyses between the optical properties (α_{mar} and β_{mar}) and wind speed of these two layers are conducted by averaging the optical properties along wind speed grids ($1\,\mathrm{m\,s^{-1}}$) and by parametric curve fitting. For the average calculations, specifically, a grid with a resolution of $1\,\mathrm{m\,s^{-1}}$ from 0 to $30\,\mathrm{m\,s^{-1}}$ is defined and the mean values as well as the standard deviations along the grid are calculated for both layers above the study areas, respectively. It should be emphasized primarily that before calculating the averages of each wind speed grid, the outliers larger or less than the average ± 1 standard deviation are eliminated. About 70 %–80 % of α_{mar} and β_{mar} are retained after the elimination. The rather strict outlier removal is conducted here to reject the data that are not representative of marine aerosol (i.e., may be contaminated by clouds, thus becoming higher than the typical range). Hence, it can guarantee the data quality and the validity of the pure marine aerosol optical properties in the statistical analysis process. Moreover, the wind speed grid with data counts less than 100 is considered unrepresentative and the statistical result of this grid is discarded. As derived data of α_{mar}, β_{mar}, averaged $\mathrm{AOD_{mar}}$, and $\mathrm{LR_{mar}}$ are obtained and discussed as well. The $\mathrm{AOD_{mar}}$ is acquired by integrating Aeolus-retrieved α_{mar} within 2 km of each single profile. The $\mathrm{AOD_{mar}}$ is calculated within the height of 2 km in order to compare it with the previous result of CALIOP, where the integration height is the same as that in this study. In Sect. 4.4.1, the averaged $\mathrm{AOD_{mar}}$ along the wind speed grid is obtained and then compared with the $\mathrm{AOD_{mar}}$–wind speed relationships from a previous study. The $\mathrm{LR_{mar}}$ is derived via dividing α_{mar} by β_{mar} for each corresponding data bin. The spatial distribution of

$\mathrm{LR_{mar}}$ is presented in Sect. 4.2, while the relationships between the variations in $\mathrm{LR_{mar}}$ along wind speed grids and the marine aerosol particle size are discussed in Sect. 4.4.2.

The procedures of the study methodology are summarized in a flowchart in Fig. 2.

4   Results and discussion

4.1   Analysis of aerosol types

To verify the dominance of marine aerosol, as discussed in Sect. 3, the CALIOP VFM aerosol classification products are applied. The proportions of eight aerosol types (marine, dusty marine, dust, polluted dust, continental, polluted continental, smoke, and others) are counted in two vertical layers defined in Sect. 3 over the NP area, the SP area, and the SI area, respectively, as shown in the histograms in Fig. 3. The proportions of marine aerosol at $\mathrm{Layer_L}$ in these three separate areas are 87 %, 84 %, and 84 %, while the proportions at $\mathrm{Layer_H}$ are 84 %, 79 %, and 79 %, respectively, which are all larger than 75 %. Moreover, the sums of the percentage of marine aerosol and dusty marine aerosol are all above 90 % for both layers and for all study areas. Consequently, the selected areas NP, SP, and SI can be considered as the marine aerosol dominating areas. It should be noted that "dusty marine", an aerosol subtype introduced for the first time in version 4.10 of the CALIOP VFM product, was not present in version 3.41 and was identified from part of the "polluted dust" of version 3.41 with the criteria of "surface type" and "layer base altitude". The use of version 3.41 of the CALIOP VFM data for the period from 19 January 2022 to 4 July 2022 led to the underestimation of the "dusty marine" fraction and the total marine aerosol fraction. Even though, under the condition of underestimation, the percentage of total marine aerosol is larger than 90 %, which means that the real proportion of total marine aerosol is higher, the conclusion that marine aerosol dominates in the altitude range of 0–2 km above these three areas is still valid.

In this section, with the statistical analyses of aerosol types, the dominance of marine aerosol is confirmed in these three areas. It should be noted that among the areas, the NP area is mainly located at low latitudes or in the tropics, while the SP area and the SI area are located in mid-latitude regions.

4.2   Spatial distribution of wind speed and aerosol optical properties

With the Aeolus Level-2A product (particle optical properties) and Level-2C product (ECMWF model winds) from April 2020 to July 2022, calculated for each $5° \times 5°$ grid, the averaged wind speed, α_{mar}, β_{mar}, and $\mathrm{LR_{mar}}$ spatial distributions of $\mathrm{Layer_H}$ and $\mathrm{Layer_L}$ are acquired.

Figures 4–6 present the averaged spatial distributions of atmospheric parameters at two layers above the NP area, the SP
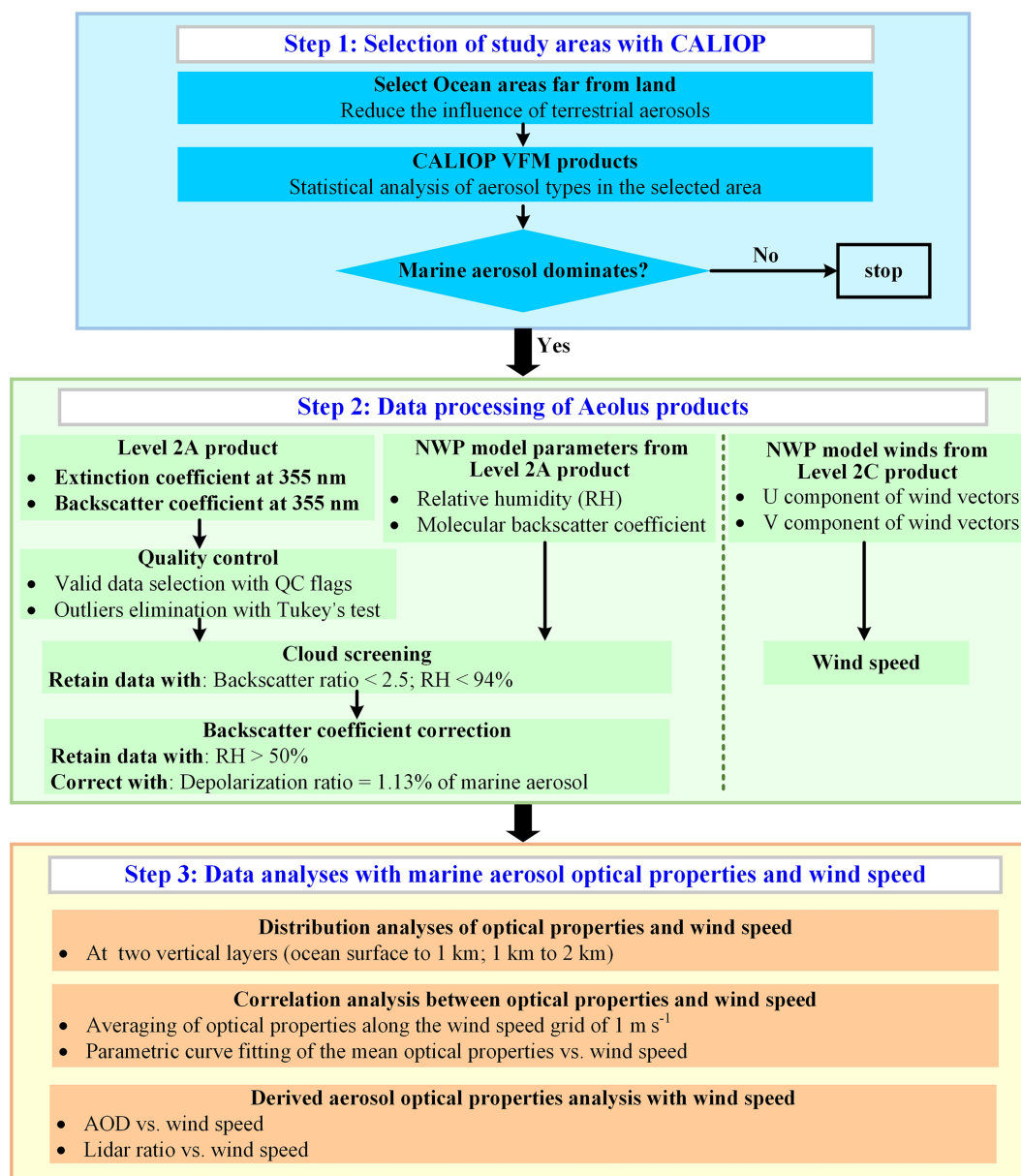
Step 1: Selection of study areas with CALIOP

Select Ocean areas far from land
Reduce the influence of terrestrial aerosols

CALIOP VFM products
Statistical analysis of aerosol types in the selected area

Marine aerosol dominates? — No → stop

Yes

Step 2: Data processing of Aeolus products

Level 2A product
- **Extinction coefficient at 355 nm**
- **Backscatter coefficient at 355 nm**

NWP model parameters from Level 2A product
- Relative humidity (RH)
- Molecular backscatter coefficient

NWP model winds from Level 2C product
- U component of wind vectors
- V component of wind vectors

Quality control
- Valid data selection with QC flags
- Outliers elimination with Tukey's test

Cloud screening
Retain data with: Backscatter ratio < 2.5; RH < 94%

Wind speed

Backscatter coefficient correction
Retain data with: RH > 50%
Correct with: Depolarization ratio = 1.13% of marine aerosol

Step 3: Data analyses with marine aerosol optical properties and wind speed

Distribution analyses of optical properties and wind speed
- At two vertical layers (ocean surface to 1 km; 1 km to 2 km)

Correlation analysis between optical properties and wind speed
- Averaging of optical properties along the wind speed grid of $1\,\mathrm{m\,s^{-1}}$
- Parametric curve fitting of the mean optical properties vs. wind speed

Derived aerosol optical properties analysis with wind speed
- AOD vs. wind speed
- Lidar ratio vs. wind speed

Figure 2. Flowchart of the study methodology.

area, and the SI area. These figures describe the atmospheric background state of optical properties and wind speed within (Layer$_L$) and above (Layer$_H$) the MABL over the study areas. Primarily, the spatial variations in wind speed, α_{mar}, and β_{mar} are more apparent along the meridian than zonally, both at Layer$_H$ and at Layer$_L$. In the aspect of Layer$_L$, there are separate distinct high wind speed regions or belts along the latitude in the three areas, which are the 5–20° N region of the NP area with the wind speed bins from approximately $8\,\mathrm{m\,s^{-1}}$ to more than $10\,\mathrm{m\,s^{-1}}$, the 40–60° S region of the SP area with the wind speed bins from more than $10\,\mathrm{m\,s^{-1}}$ to approximately $17\,\mathrm{m\,s^{-1}}$, and the 35–60° S region of the SI area with the wind speed bins from more than $10\,\mathrm{m\,s^{-1}}$ to

approximately $17\,\mathrm{m\,s^{-1}}$ as well. Inspection of marine aerosol optical properties, α_{mar}, and β_{mar} in the high wind speed regions are obviously larger than in other regions. Hence, it can be inferred that, in the MABL, the wind speed and the marine aerosol optical properties tend to be positively correlated. Referring to Layer$_H$, shown in the upper four panels of Figs. 4–6, it can be seen that the spatial variation trends of wind speed, α_{mar}, and β_{mar} in the three areas are similar to those at Layer$_L$. The apparent high wind speed regions, where the wind speeds are up to around $8–10\,\mathrm{m\,s^{-1}}$ in 5–20° N of the NP area, $15–18\,\mathrm{m\,s^{-1}}$ in 40–60° S of the SP area, and $13–19\,\mathrm{m\,s^{-1}}$ in 35–60° S of the SI area, also exist at Layer$_H$, while α_{mar} and β_{mar} are slightly enhanced in
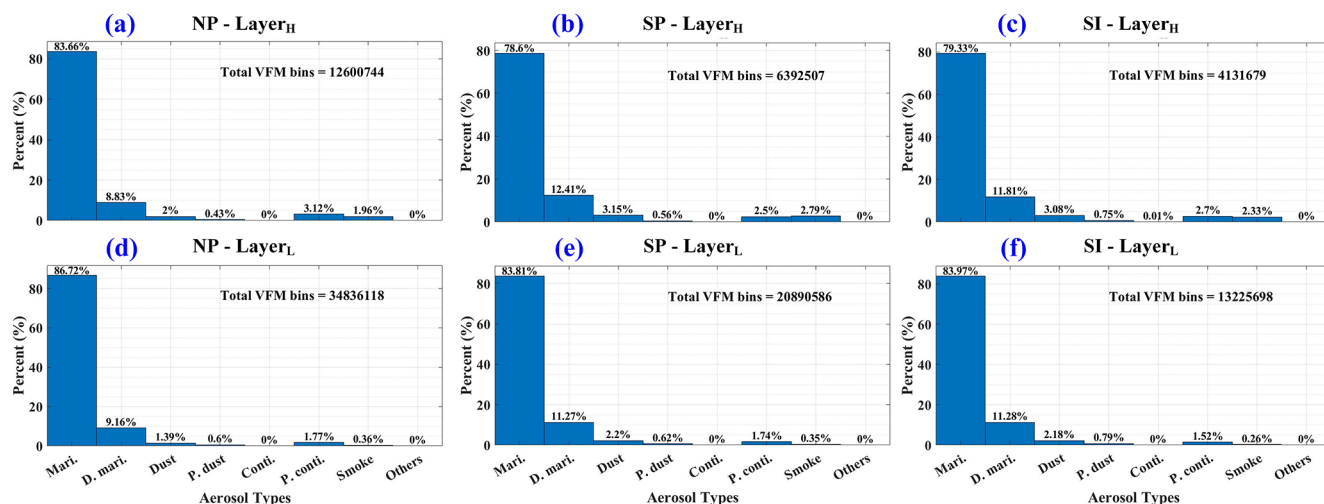
Figure 3. Statistical analyses of aerosol types over the NP area **(a, d)**, the SP area **(b, e)**, and the SI area **(c, f)** at two separate layers.
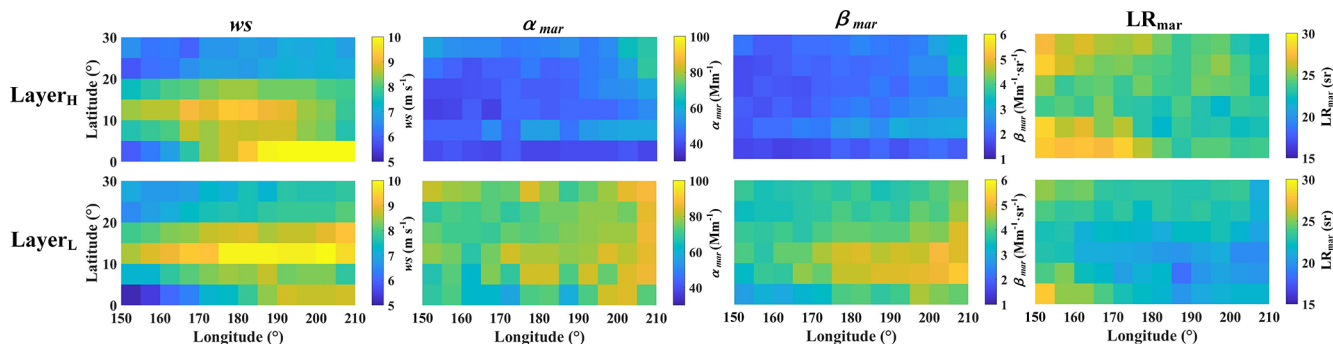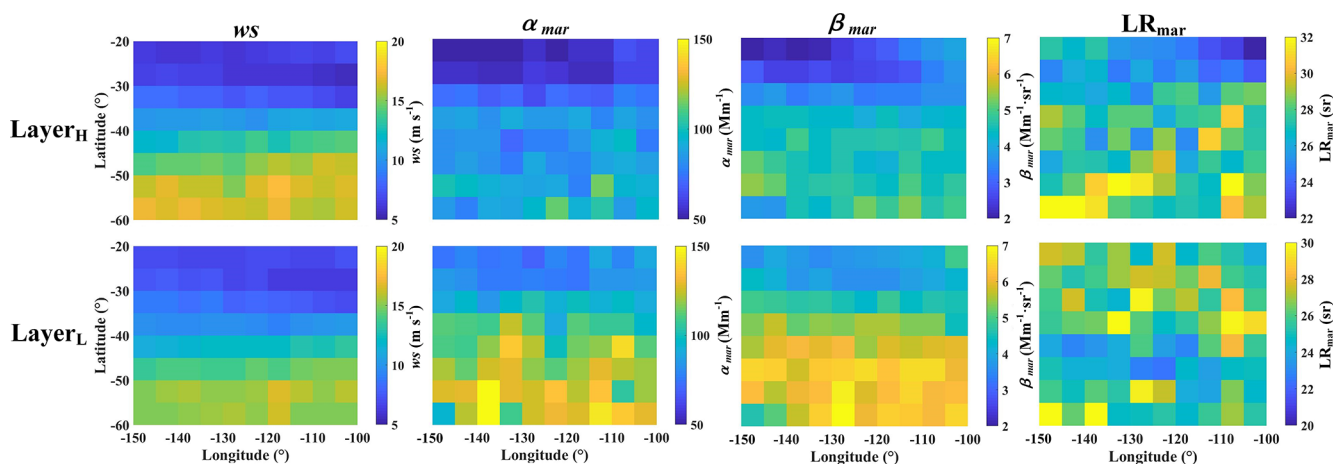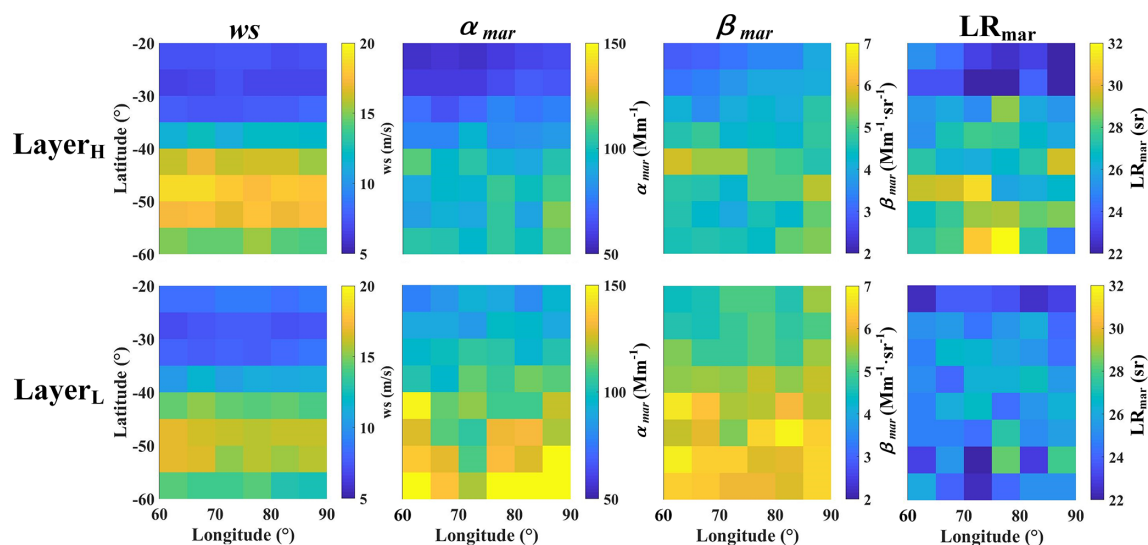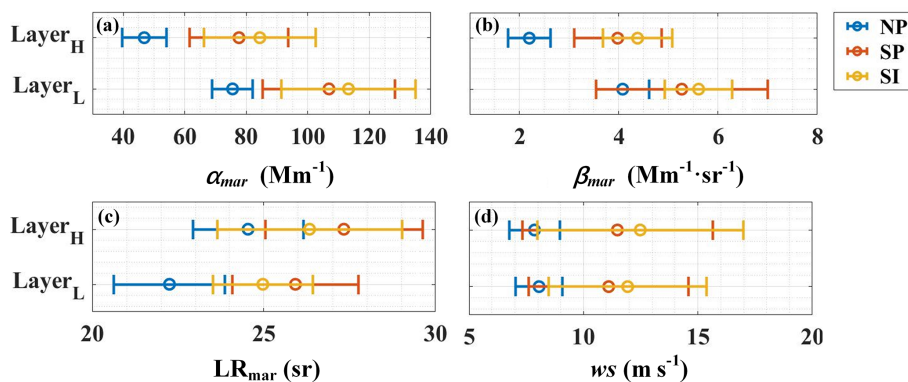

Figure 4. Wind speed (ws), marine aerosol extinction coefficient (α_{mar}), marine aerosol backscatter coefficient (β_{mar}), and marine aerosol lidar ratio ($\mathrm{LR}_{\mathrm{mar}}$) spatial distributions above the North Pacific (NP) area at $\mathrm{Layer_H}$ and $\mathrm{Layer_L}$.

Figure 5. Wind speed (ws), marine aerosol extinction coefficient (α_{mar}), marine aerosol backscatter coefficient (β_{mar}), and marine aerosol lidar ratio ($\mathrm{LR}_{\mathrm{mar}}$) spatial distributions above the South Pacific (SP) area at $\mathrm{Layer_H}$ and $\mathrm{Layer_L}$.

Figure 6. Wind speed (ws), marine aerosol extinction coefficient (α_{mar}), marine aerosol backscatter coefficient (β_{mar}), and lidar ratio (LR_{mar}) spatial distributions above the South Indian (SI) area at Layer$_H$ and Layer$_L$.

these regions which indicates that the wind speed may still have a weak positive influence on the marine aerosol optical properties at the higher atmospheric layer above the MABL. Some differences in the spatial distribution of wind speed, α_{mar}, and β_{mar} between the three areas can be discovered as well. As for the SP area and the SI area, wind speed, α_{mar}, and β_{mar} all mainly present increasing tendencies from north to south. In terms of the NP area, besides the obvious enhancements of wind speed, α_{mar}, and β_{mar} in the high wind speed belt, the gradual enhancements of these atmospheric parameters from west to east are presented in this area.

At both layers of the NP area and at Layer$_L$ of the SP area, the LR_{mar} turns out lower in the relatively high wind speed regions, which illustrates a possible negative correlation between LR_{mar} and wind speed. The relationship between these two parameters is analyzed and discussed in detail in Sect. 4.4.2.

Additionally, the mean values and the standard deviations of these atmospheric parameters at Layer$_H$ and Layer$_L$ are calculated for each study area by averaging the spatial distributions of the $5° \times 5°$ grid, and are presented in Fig. 7. The averaged wind speed values are 8.1 ± 1.0, 11.1 ± 3.5, and $12.0 \pm 3.5 \, \text{m s}^{-1}$ at Layer$_L$, while 7.9 ± 1.1, 11.5 ± 4.2, and $12.5 \pm 4.5 \, \text{m s}^{-1}$ at Layer$_H$, above the NP area, the SP area, and the SI area, respectively. The averaged α_{mar} values are 76 ± 7, 107 ± 22, $113 \pm 22 \, \text{Mm}^{-1}$ at Layer$_L$, while 47 ± 7, 78 ± 16, $84 \pm 18 \, \text{Mm}^{-1}$ at Layer$_H$, above the NP area, the SP area, and the SI area, respectively. The averaged β_{mar} values are 4.1 ± 0.5, 5.3 ± 1.7, and $5.6 \pm 0.7 \, \text{Mm}^{-1} \, \text{sr}^{-1}$ at Layer$_L$, while 2.2 ± 0.4, 4.0 ± 0.9, and $4.4 \pm 0.7 \, \text{Mm}^{-1} \, \text{sr}^{-1}$ at Layer$_H$, above the NP area, the SP area, and the SI area, respectively. The averaged LR_{mar} values are 22.3 ± 1.6, 25.9 ± 1.8, and 25.0 ± 1.5 sr at Layer$_L$, while 24.5 ± 1.6,

27.3 ± 2.3, and 26.3 ± 2.7 sr at Layer$_H$, above the NP area, the SP area, and the SI area, respectively. It is reported that the typical ranges of α_{mar} and β_{mar} at 532 nm over remote ocean areas are around 60–$80 \, \text{Mm}^{-1}$ and around 1–$5 \, \text{Mm}^{-1} \, \text{sr}^{-1}$, respectively, as observed and retrieved by CALIOP (Prijith et al., 2014; Kiliyanpilakkil and Meskhidze, 2011). Applying the typical α_{mar} Ångström exponent from 532 to 355 nm of 0.7 ± 1.3 and the typical β_{mar} Ångström exponent from 532 to 355 nm of 0.8 ± 0.1 (Floutsi et al., 2023), the converted typical ranges of α_{mar} and β_{mar} at 355 nm can be calculated, which are around 47–$180 \, \text{Mm}^{-1}$ and around 1.3–$7.2 \, \text{Mm}^{-1} \, \text{sr}^{-1}$. Compared with the typical ranges of α_{mar} and β_{mar} at 355 nm, calculated from CALIOP-retrieved typical ranges of marine aerosol optical properties and the typical conversion coefficients, the Aeolus-retrieved α_{mar} and β_{mar} are considered reasonable. The mean values of wind speed, α_{mar}, and β_{mar} above the NP area are the lowest among the three areas, both at Layer$_H$ and Layer$_L$, which may be because that area is located in the low latitude region of the Northern Hemisphere. The highest mean wind speed of the SI area corresponds to the highest α_{mar} and β_{mar}. The mean wind speeds of Layer$_H$ are both larger than those of Layer$_L$ in the SP area and in the SI area, while the phenomenon is opposite in the NP area. It is worth noting that in all the study areas, the averaged α_{mar} and β_{mar} at Layer$_L$ are larger than those at Layer$_H$, illustrating that the majority of the aerosol from oceans is trapped in the MABL, while a fraction of the marine aerosol can be elevated above the MABL. In terms of the averaged LR_{mar}, the values at Layer$_H$ are all higher than those at Layer$_L$, and all the values are within a reasonable range with reference to those reported by Bohlmann et al. (2018), Groß et al. (2011, 2015), and Floutsi et al. (2023).

Figure 7. Mean values at $Layer_H$ and $Layer_L$ of **(a)** marine aerosol extinction coefficient (α_{mar}), **(b)** marine aerosol backscatter coefficient (β_{mar}), **(c)** marine aerosol lidar ratio (LR_{mar}), and **(d)** wind speed (ws) above the North Pacific (NP) area (blue standard deviation bars), the South Pacific (SP) area (red standard deviation bars), and the South Indian (SI) area (yellow standard deviation bars).

In conclusion, this section presents the atmospheric background state of optical properties and wind speed, as well as analyzes the spatial distributions of wind speed, α_{mar}, and β_{mar} jointly at $Layer_H$ and $Layer_L$, above the NP area, the SP area, and the SI area, respectively. The α_{mar} and β_{mar} retrieved from Aeolus Level-2A products are in reasonable agreement with CALIOP, and the Aeolus-derived LR_{mar} values are also reasonable. It is found that, both at $Layer_H$ and at $Layer_L$, spatially, the wind speed, α_{mar}, and β_{mar} show positive correlation, though the optical properties at $Layer_L$ are greater than those at $Layer_H$ indicating that both layers receive the input of the aerosol produced from the ocean by the wind but the majority of the marine aerosol is trapped in the MABL and only a small fraction can be elevated into the higher layer. In addition, as the three study areas are located in different regions, the spatial distributions of wind speed, α_{mar}, and β_{mar} are different.

4.3 Relationship between marine aerosol optical properties and wind speed

In order to determine the relationship between the marine aerosol optical properties and the corresponding wind speed, utilizing the method introduced in Sect. 3, the mean values and standard deviations (after outlier removal) of α_{mar} and β_{mar}, along with the wind speed grid at two layers above the NP area, the SP area, and the SI area, are shown in panels (a) and (b) of Figs. 8–10, respectively. The regression curves of the optical properties are presented in these figures as well. The power-law function is used for curve fitting to describe the trend of marine aerosol optical properties with wind speed. In addition, the data counts in each wind speed grid are shown as the histograms in panels (a) and (b) of Figs. 8–10. In order to illustrate the variation tendencies of α_{mar} and β_{mar}, the slopes of α_{mar} and β_{mar} with wind speed are also provided in panels (c) and (d) of Figs. 8–10. Table 1 summarizes the regression functions together with the corre-

sponding R^2, and the proportions of the different wind speed bins together with the count sums, grouped by area, layer, and optical property.

From the statistical results with wind speed grids and wind speed ranges, it can be found that most of the wind speeds are below $15\,\mathrm{m\,s^{-1}}$ above the NP area, both at $Layer_H$ and $Layer_L$, while the proportion of low wind speed ($0 < \mathrm{ws} \leq 8\,\mathrm{m\,s^{-1}}$) is slightly higher at $Layer_H$ than at $Layer_L$. As for the SP area and the SI area, the proportions of high wind speed ($\mathrm{ws} > 15\,\mathrm{m\,s^{-1}}$) account for around one-fifth to one-quarter, respectively, and the proportion of low wind speed over the SP area is higher than that over the SI area. The wind speed distribution is more concentrated at $Layer_L$ than at $Layer_H$ above these two areas, in view of the lower proportion of low and high wind speeds and the higher proportion of medium wind speeds ($8 < \mathrm{ws} \leq 15\,\mathrm{m\,s^{-1}}$) at $Layer_L$.

Generally, in all cases shown in Figs. 8–10, the optical properties at $Layer_L$ are all larger than those at $Layer_H$ in the same wind speed grid, while with the variations in the marine aerosol optical properties along the wind speed grid it can be clearly observed that the tendency is increasing with the wind speed. Moreover, the regression curves are fitted pretty well as the R^2 are all above 0.90.

As Fig. 8a and b show, in the NP area, α_{mar} at $Layer_L$ increases from $64\,\mathrm{Mm^{-1}}$ at the 0–$1\,\mathrm{m\,s^{-1}}$ wind speed interval to $113\,\mathrm{Mm^{-1}}$ at the 16–$17\,\mathrm{m\,s^{-1}}$ wind speed interval, while at $Layer_H$ it increases from $42\,\mathrm{Mm^{-1}}$ at the 0–$1\,\mathrm{m\,s^{-1}}$ wind speed interval to $57\,\mathrm{Mm^{-1}}$ at the 17–$18\,\mathrm{m\,s^{-1}}$ wind speed interval; β_{mar} at $Layer_L$ increases from $2.2\,\mathrm{Mm^{-1}\,sr^{-1}}$ at the 0–$1\,\mathrm{m\,s^{-1}}$ wind speed interval to $6.6\,\mathrm{Mm^{-1}\,sr^{-1}}$ at the 16–$17\,\mathrm{m\,s^{-1}}$ wind speed interval, while at $Layer_H$ it increases from $1.6\,\mathrm{Mm^{-1}\,sr^{-1}}$ at the 0–$1\,\mathrm{m\,s^{-1}}$ wind speed interval to $3.3\,\mathrm{Mm^{-1}\,sr^{-1}}$ at the 17–$18\,\mathrm{m\,s^{-1}}$ wind speed interval. The increments of these two parameters at $Layer_L$ are much larger than those at $Layer_H$. Moreover, the exponents of the regression functions are all greater than 1, indicating that the growth rates of the optical properties increase along the wind
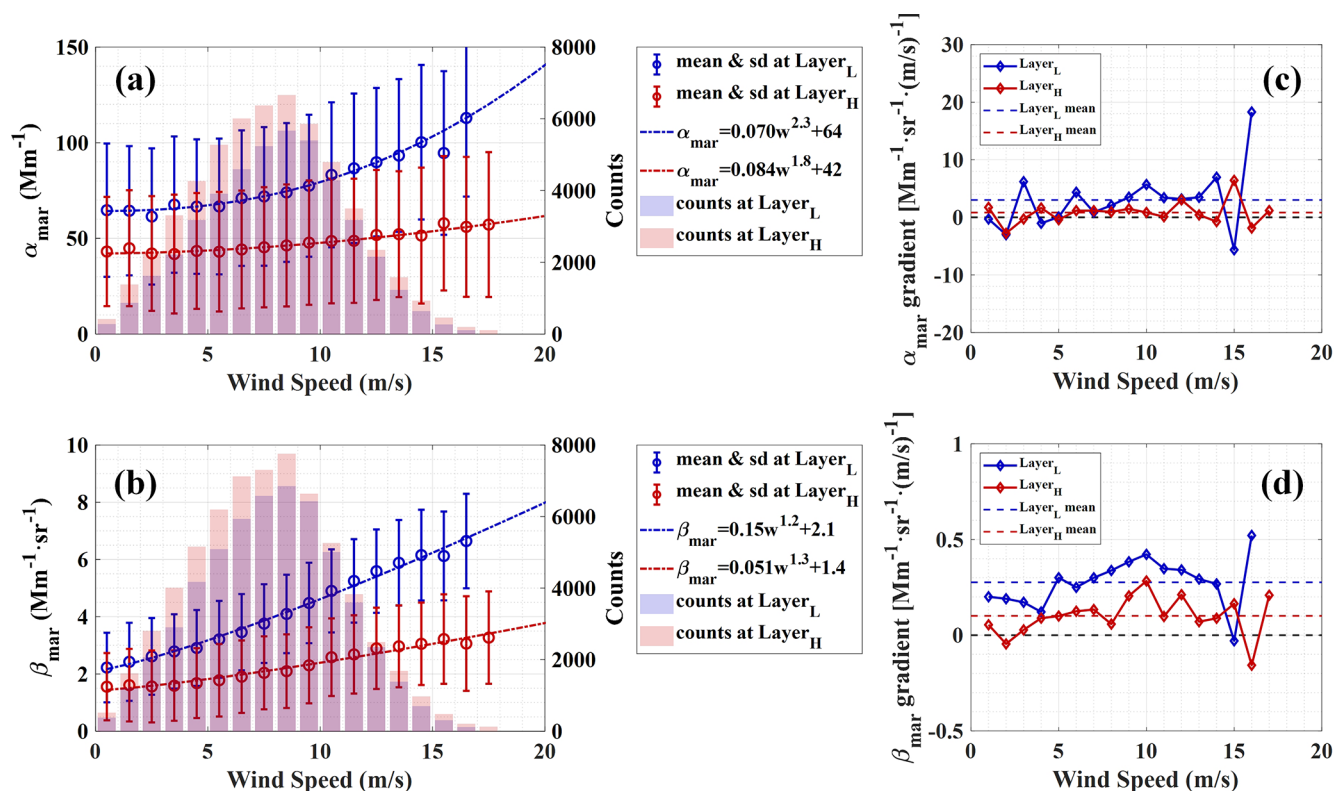
Figure 8. Relationship between marine aerosol optical properties ((**a**) for α_{mar} and (**b**) for β_{mar}) and wind speed above the NP area. The blue circles and error bars represent the means and standard deviations of the optical properties along wind speed grids at $Layer_L$, while the reds represent the same items at $Layer_H$. The dotted–dashed blue and red lines are the optical property average regression curves fitted along the wind speed grid at $Layer_L$ and $Layer_H$, respectively. The blue and red histograms indicate the data counts of every wind speed grid at $Layer_L$ and $Layer_H$, respectively. Panels (**c**) and (**d**) represent the slopes of α_{mar} and β_{mar} with wind speed at $Layer_L$ (blue lines) and $Layer_H$ (red lines), respectively, while the dashed blue lines and the dashed red lines show the mean values of the slopes at two layers.

Table 1. Regression functions of the averaged optical properties and the wind speed grids, together with the corresponding wind speed distributions, grouped by area and layer.

| Area	Layer	Optical property	Regression function	R^2	Proportion of wind speed bins ($\mathrm{m\,s^{-1}}$)			Number of counts
					$0 < \mathrm{ws} \le 8$	$8 < \mathrm{ws} \le 15$	$\mathrm{ws} > 15$	
NP	H	α_{mar}	$\alpha_{mar} = 0.084 \cdot \mathrm{ws}^{1.8} + 42$	0.95	0.53	0.46	0.01	55 758
		β_{mar}	$\beta_{mar} = 0.050 \cdot \mathrm{ws}^{1.3} + 1.4$	0.97	0.54	0.45	0.01	64 191
	L	α_{mar}	$\alpha_{mar} = 0.070 \cdot \mathrm{ws}^{2.3} + 64$	0.99	0.49	0.50	0.01	44 857
		β_{mar}	$\beta_{mar} = 0.15 \cdot \mathrm{ws}^{1.2} + 2.1$	0.99	0.51	0.48	0.01	55 117
SP	H	α_{mar}	$\alpha_{mar} = 5.0 \cdot \mathrm{ws}^{0.84} + 54$	0.95	0.46	0.34	0.20	34 088
		β_{mar}	$\beta_{mar} = 1.3 \cdot \mathrm{ws}^{0.48} + 1.1$	0.96	0.49	0.31	0.20	30 348
	L	α_{mar}	$\alpha_{mar} = 6.1 \cdot \mathrm{ws}^{0.83} + 73$	0.98	0.45	0.38	0.17	25 783
		β_{mar}	$\beta_{mar} = 1.8 \cdot \mathrm{ws}^{0.47} + 1.1$	0.97	0.47	0.36	0.17	23 854
SI	H	α_{mar}	$\alpha_{mar} = 0.65 \cdot \mathrm{ws}^{1.4} + 56$	0.95	0.40	0.35	0.25	19 552
		β_{mar}	$\beta_{mar} = 0.60 \cdot \mathrm{ws}^{0.59} + 1.7$	0.96	0.42	0.33	0.25	16 473
	L	α_{mar}	$\alpha_{mar} = 1.1 \cdot \mathrm{ws}^{1.2} + 81$	0.92	0.38	0.41	0.21	15 953
		β_{mar}	$\beta_{mar} = 1.2 \cdot \mathrm{ws}^{0.47} + 1.7$	0.97	0.46	0.36	0.18	13 923
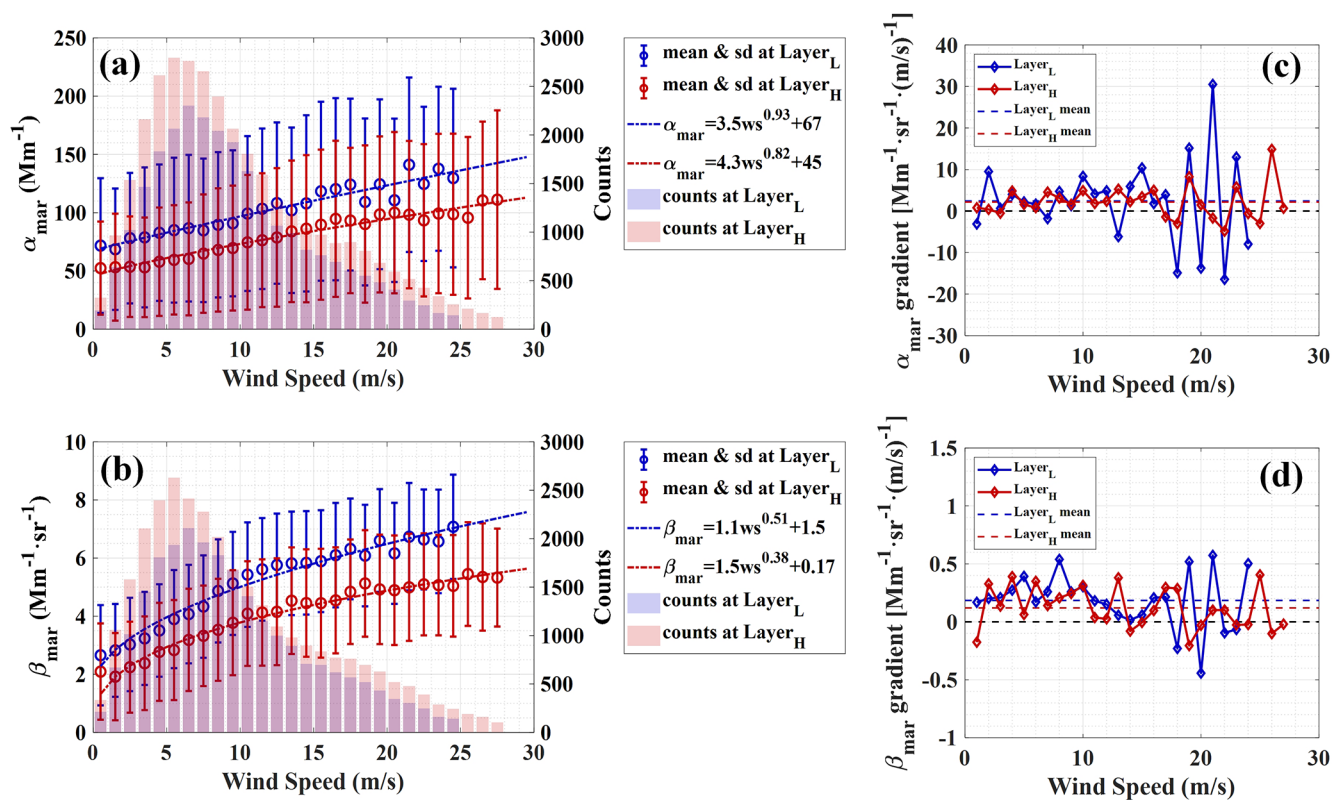
Figure 9. Relationship between marine aerosol optical properties and wind speed above the SP area. The items represent the same as those of Fig. 8.

grid. Referring to Fig. 8c and d, the mean values of the slopes of α_{mar} and β_{mar} at $Layer_L$ are higher than those at $Layer_H$. Furthermore, the slopes at $Layer_L$ are mostly larger than those at $Layer_H$ within the same wind speed interval, i.e., the optical properties at $Layer_L$ will increase more rapidly with wind speed. It is worth noting that for the case where the wind speed is above $10\,m\,s^{-1}$, the slopes of β_{mar} show decreasing tendencies, whereas for the condition where the wind speed is lower than $10\,m\,s^{-1}$, the values of the β_{mar} slopes present increasing tendencies, indicating the better fitting by power-law functions at lower wind speeds. This phenomenon implies that there might be two distinct variation trends in β_{mar} above and below the wind speed of $10\,m\,s^{-1}$.

For the SP area and the SI area, the maximum wind speed can reach up to $28\,m\,s^{-1}$, while the variation in the optical properties along with wind speed is more complicated. In Fig. 9a, the α_{mar} values over the SP area show approximately linear growth tendencies with wind speed both at $Layer_L$ and at $Layer_H$, with the exponents of the fitting functions of 0.93 and 0.82. The α_{mar} values increase from 72 and 52 Mm^{-1} to 130 and 111 Mm^{-1} for $Layer_L$ and $Layer_H$, respectively. Figure 9b shows that the β_{mar} above the SP area increases from 2.7 and 2.1 $Mm^{-1}\,sr^{-1}$ to 7.0 and 5.3 $Mm^{-1}\,sr^{-1}$, with the exponents of the fitting functions of 0.51 and 0.38 for $Layer_L$ and $Layer_H$. From Fig. 10a and b, it can be seen that

the variations in α_{mar} and β_{mar} with wind speed in the SI area are similar to those in the SP area, except for that the exponents of the fitting functions of β_{mar} are larger than 1, i.e., 1.2 and 1.4 for $Layer_L$ and $Layer_H$, respectively. In $Layer_H$ of the SI area, α_{mar} at above $25\,m\,s^{-1}$ can reach up to $137\,Mm^{-1}$, much larger than that of around $110\,Mm^{-1}$ in the SP area. Panels (c) and (d) of Figs. 9 and 10 show the slopes of α_{mar} and β_{mar} with the wind speed above the SP area and the SI area. In these four panels, the dashed blue lines (mean values of the slopes at $Layer_L$) are all higher than the dashed red lines (mean values of the slopes at $Layer_H$), illustrating that the increments of α_{mar} and β_{mar} per unit of wind speed at $Layer_L$ are larger than those at $Layer_H$, which implies that the input of marine aerosol driven by wind at $Layer_L$ is stronger than at $Layer_H$. Focusing on Figs. 9c and 10c, it can be seen that, for both layers of the SP area and the SI area, the slopes of α_{mar} below $15\,m\,s^{-1}$ are almost all larger than 0, fluctuating slightly around the mean values, while the slopes of α_{mar} above $15\,m\,s^{-1}$ fluctuate drastically. This phenomenon may indicate that below $15\,m\,s^{-1}$, both layers continuously receive the input of marine aerosol driven by wind, but nevertheless, when the wind speed is higher than $15\,m\,s^{-1}$, the dependence of marine aerosol on wind becomes lower. As for the slopes of β_{mar} above the SP area and the SI area, from Figs. 9d and 10d, it is obvious that for both layers, the
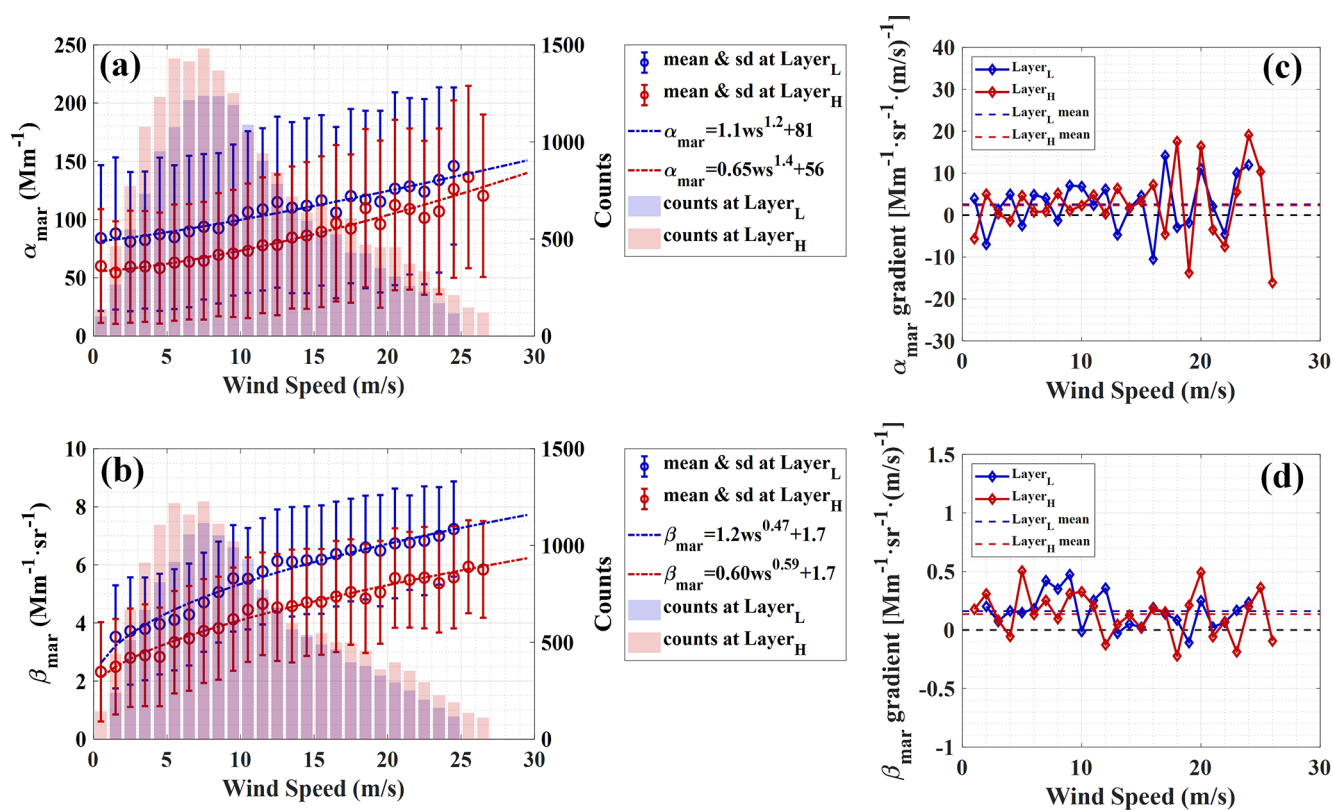
Figure 10. Relationship between marine aerosol optical properties and wind speed above the SI area. The items represent the same as those of Fig. 8.

slopes of β_{mar} decrease above around $10\,\mathrm{m\,s^{-1}}$. The corresponding variations in β_{mar} above the SP area and the SI area are shown in Figs. 9b and 10b, of which the β_{mar} values increase with higher slopes at the wind speed range of 0–$10\,\mathrm{m\,s^{-1}}$, while the slopes of increase become lower when the wind speed is above $10\,\mathrm{m\,s^{-1}}$. This phenomenon might indicate that the increase in β_{mar} with wind speed includes two separate trends regarding $10\,\mathrm{m\,s^{-1}}$ as the change point, consistent with the hypothesis raised in the analysis of the NP area. We name these two wind speeds ($15\,\mathrm{m\,s^{-1}}$ for α_{mar} and $10\,\mathrm{m\,s^{-1}}$ for β_{mar}) "slope variation points" in this paper. Table 2 presents the averaged slopes (mean) and the corresponding standard deviations of α_{mar} and β_{mar}, below and above the slope variation points, for the two layers of the SP and SI areas. All the averaged slopes below the slope variation points are larger than those above the slope variation points, except for the α_{mar} in the SI area. The reason for the inverse results of α_{mar} in the SI area may be due to its rapid increase above $24\,\mathrm{m\,s^{-1}}$. All standard deviations of β_{mar} above the slope variation points are greater than those below, indicating a more fluctuating growth phase above the slope variation points. These results could provide evidence for the statement that the wind-driven enhancement of marine aerosol includes two phases: a rapid-growth phase

with high wind dependence and a slower-growth phase with higher fluctuations.

Consequently, for all measurement cases, the marine aerosol optical properties at $\mathrm{Layer_L}$ are larger than those at $\mathrm{Layer_H}$ in any identical wind speed interval, indicating that the MABL may receive more marine aerosol produced and transported from the sea–air interface, while the higher layer above the MABL with the upper boundary of $2\,\mathrm{km}$ can also be affected by the marine aerosol, but to a lesser extent. The mean slope values of α_{mar} and β_{mar} at $\mathrm{Layer_L}$ are all larger than at $\mathrm{Layer_H}$, which implies that the marine aerosol enhancements caused by the background wind are more intense at the MABL. It should be noted that the slopes change as α_{mar} and β_{mar} increase with wind speed. The slope variation point of α_{mar} ($15\,\mathrm{m\,s^{-1}}$) is greater than that of β_{mar} ($10\,\mathrm{m\,s^{-1}}$), and above it the enhancement rate becomes lower. This could illustrate that the impact of wind on marine aerosol enhancement includes two phases, one of which is a rapid-growth phase with a high dependence on wind and the other is a slower-growth phase with more fluctuations after the slope variation points.

Table 2. Mean ± SD of the slopes below and above the slope variation point, grouped by area and layer.

Optical property	Area	Layer	Mean ± SD of the slopes [Mm^{-1} (m s^{-1})$^{-1}$ for α_{mar}, Mm^{-1} sr^{-1} (m s^{-1})$^{-1}$ for β_{mar}]	
			Below slope variation point	Above slope variation point
α_{mar}	SP	H	2.48 ± 1.81	1.79 ± 5.71
		L	3.11 ± 4.62	1.26 ± 16.11
	SI	H	1.96 ± 3.10	2.81 ± 12.59
		L	2.16 ± 4.28	3.28 ± 8.79
β_{mar}	SP	H	0.20 ± 0.17	0.07 ± 0.17
		L	0.28 ± 0.11	0.12 ± 0.29
	SI	H	0.21 ± 0.16	0.09 ± 0.20
		L	0.22 ± 0.16	0.12 ± 0.13

4.4 Dependency of aerosol optical depth and lidar ratio on wind speed

4.4.1 Marine aerosol optical depth versus wind speed

As introduced in Sect. 1, almost all the previous studies on the relationship between marine aerosol optical properties and wind speed have focused on the AOD of marine aerosol. In this study, an attempt on the averaged 0–2 km AOD$_{mar}$ of individual wind speed grid calculation has also been conducted to compare the AOD$_{mar}$–wind speed relationship from a previous study (Kiliyanpilakkil and Meskhidze, 2011). The AOD$_{mar}$ of each single profile is acquired by integrating Aeolus-retrieved α_{mar} within 2 km. The wind speed profiles are also averaged over 2 km to match the AOD$_{mar}$ data. Then the relationship between the AOD$_{mar}$ and the wind speeds is obtained by averaging the AOD$_{mar}$ in each wind speed interval (0–30 m s^{-1}, stepped by 1 m s^{-1}). The AOD$_{mar}$–wind speed relationship is also investigated using the products from the A-Train satellites (Kiliyanpilakkil and Meskhidze, 2011). "Clean marine" aerosol AOD at 532 nm above the ocean surface (up to 2 km) provided by CALIOP, and 10 m daily wind speed provided by AMSR-E, were used. It should be noted that the wind speed used in Kiliyanpilakkil and Meskhidze (2011) is the daily ocean surface wind speed, different from that used in this study, which is the instantaneous layer-averaged wind speed. Collecting the data for the period from 2006 to 2011 over 15 remote ocean regions worldwide, the regression curve is acquired with the averaged AOD$_{mar}$ at 532 nm for each wind speed grid and the surface wind speed, which is up to 29 m s^{-1}, and the regression function is expressed as shown in Eq. (3):

$$\mathrm{AOD}_{mar,532} = \frac{0.15}{1 + 6.7 \cdot e^{-0.17 \cdot U_{10}}}, \tag{3}$$

where U_{10} represents the daily 10 m ocean surface wind speed.

As described above, the AOD$_{mar}$'data source (from spaceborne lidar observations), the study areas (remote ocean regions globally), and the wind speed range (0–29 m s^{-1}) of

the AOD$_{mar}$–wind speed relationship exploration in Kiliyanpilakkil and Meskhidze (2011) match well with those of this study. Hence, we select the AOD$_{mar}$–wind speed relationship established by Kiliyanpilakkil and Meskhidze (2011) for comparison. Additionally, due to the different wavelengths of AOD$_{mar}$ used in this study (355 nm) and in Kiliyanpilakkil and Meskhidze (2011) (532 nm), the conversion of the AOD$_{mar}$ at 532 nm to the AOD$_{mar}$ at 355 nm is performed by applying the typical Ångström exponent of marine aerosol. It is reported that the Ångström exponent of marine aerosol is related to the surface wind speed, and a linear relationship has been established as given in Eq. (4) (Sayer et al., 2012):

$$A(\mathrm{ws}) = 0.69 - 0.030 \cdot \mathrm{ws}, \tag{4}$$

where A represents the Ångström exponent and ws represents the wind speed. Then the AOD$_{mar}$ at 532 nm can be converted to the AOD$_{mar}$ at 355 nm by Eq. (5):

$$\mathrm{AOD}_{mar,355\,nm}(\mathrm{ws}) = \exp\left[A(\mathrm{ws}) \cdot \ln\frac{532}{355}\right] \cdot \mathrm{AOD}_{mar,532\,nm}(\mathrm{ws}). \tag{5}$$

In Fig. 11, the averaged AOD$_{mar}$ and corresponding standard deviations at 355 nm of all three study areas along the wind speed grid are represented by the blue squares and error bars, while the regression curve of AOD$_{mar}$ at 355 nm versus wind speed converted from Eq. (3) is represented by the red squares and line. Although instantaneous layer-averaged wind speed and the daily ocean surface wind speed are used in this study and in Kiliyanpilakkil and Meskhidze (2011) individually, a similar trend of AOD$_{mar}$ at 355 nm versus wind speed is obtained. It can be seen that AOD$_{mar}$ increases with wind speed, and the slope of AOD$_{mar}$ becomes higher along the wind speeds when the wind speed is below 15 m s^{-1}, while the variation in AOD$_{mar}$ becomes slower above 15 m s^{-1}. The converted CALIOP AOD$_{mar}$ values are lower than the Aeolus-retrieved AOD$_{mar}$ values at 0–10 m s^{-1}. Nevertheless, the former are all in the standard
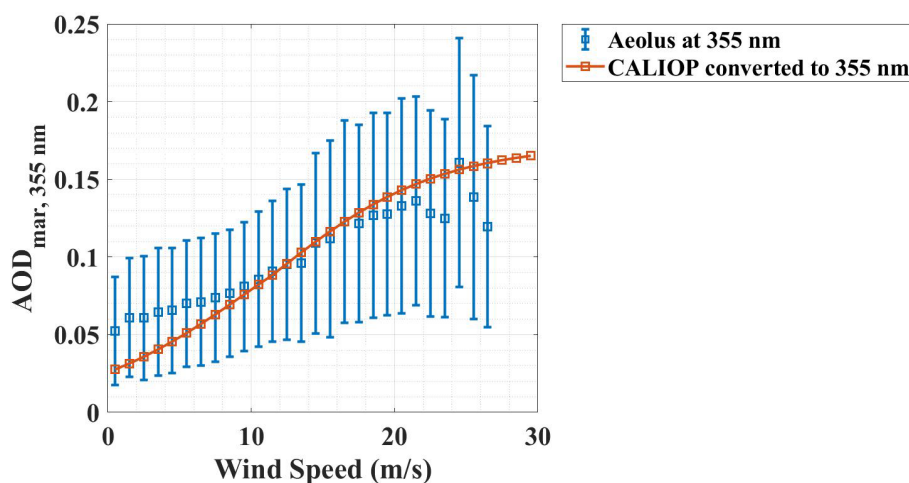
Figure 11. AOD_{mar} at 355 nm versus wind speed. The blue squares and the corresponding error bars represent the AOD_{mar} means and standard deviations along the wind speed grid of all three study areas in this study. The red squares and line represent AOD_{mar} at 355 nm along the wind speed grid converted from the regressive relationship between AOD_{mar} at 532 nm and the ocean surface wind speed reported by Kiliyanpilakkil and Meskhidze (2011).

deviation range of the latter, and thus the Aeolus-retrieved AOD_{mar} values and their variation along the wind speed are considered reasonable. The lower AOD_{mar} from CALIOP after wavelength conversion at low wind speed may arise from using a fixed LR_{mar} of 20 sr at 532 nm for CALIOP AOD_{mar} retrievals, while LR_{mar} can vary with a quite large range of 10–90 sr (Masonis et al., 2003). The possible uncertainties in the CALIOP-retrieved AOD_{mar} at 532 nm are discussed in detail in Kiliyanpilakkil and Meskhidze (2011). Furthermore, as discussed in Sect. 4.4.2 of this paper, the particle size of marine aerosol and LR_{mar} will vary with wind speed, so using the CALIOP AOD_{mar} retrieved with the fixed LR_{mar} may introduce additional error in exploring the relationship between AOD_{mar} and wind speed. Therefore, the use of Aeolus-retrieved AOD_{mar}, which is integrated by an independently retrieved extinction coefficient without the assumption of LR_{mar}, could make the AOD_{mar}–wind speed relationship more reliable.

4.4.2   Marine aerosol lidar ratio versus wind speed

As one of the intensive optical properties, LR_{mar} is independent of aerosol concentration. It is reported that LR_{mar} depends on particle size, and specifically, with the reduction in the coarse mode, the total LR turns out to increase (Masonis et al., 2003). The possible reason for this phenomenon is that as the particles become smaller, the extinction is enhanced by the increasing sideward scattering and the backscatter gets weaker due to the decrease in the scattering cross section (Haarig et al., 2017). The Aeolus Level-2A product provides the particle extinction-to-backscatter ratio calculated with the raw β, which lacks the depolarized part, as mentioned in Sect. 3. In this work, the corrected LR_{mar} is ac-

quired by dividing the marine aerosol extinction by the marine aerosol depolarization-corrected backscatter. The calculation of the averaged LR_{mar} along wind speed grids has been performed by averaging the LR_{mar} values of each $1\,\mathrm{m\,s^{-1}}$ wind speed bin, and the standard deviations are acquired as well. It should be noted that before the statistical calculations are carried out, the outliers are eliminated by the boxplot analysis method presented in Sect. 3.

In Fig. 12, 0–2 km averaged LR_{mar} variations along with the wind speed above the NP area, the SP area, and the SI area are represented as blue, red, and yellow curves, respectively. Generally, the clear downward trend of the LR_{mar} at relatively low wind speeds (0–14 $\mathrm{m\,s^{-1}}$ of the NP area, 0–9 $\mathrm{m\,s^{-1}}$ of the SP area, and 0–10 $\mathrm{m\,s^{-1}}$ of the SI area) can be observed in all cases. The results reported in this paper are similar to those of previous studies, of which Dawson et al. (2015) and Sayer et al. (2012) investigated the relationship between LR_{mar} and wind speed utilizing measured LR_{mar} and modeled LR_{mar}, respectively. Combining the corrected CALIOP-retrieved LR_{mar} at 532 nm and 10 m ocean surface wind speed from AMSR-E, the negative correlation between LR_{mar} and wind speed is acquired with the wind speed bins from 0 $\mathrm{m\,s^{-1}}$ up to $> 15\,\mathrm{m\,s^{-1}}$, shown as the purple curve in Fig. 12 (Dawson et al., 2015). The modeled LR_{mar} at 355 and at 532 nm also presents decreasing trends with the wind speed increases, presented as the green curve and the light blue curve in Fig. 12 (Sayer et al., 2012). These results seem to imply that the particle size of marine aerosol becomes larger as the wind speed increases for a low wind speed range. This phenomenon is explained by the shift in the volume size distribution of marine aerosol with wind speed: as wind speed increases, the fine mode volume size distribution of marine aerosol declines, while the coarse mode dis-
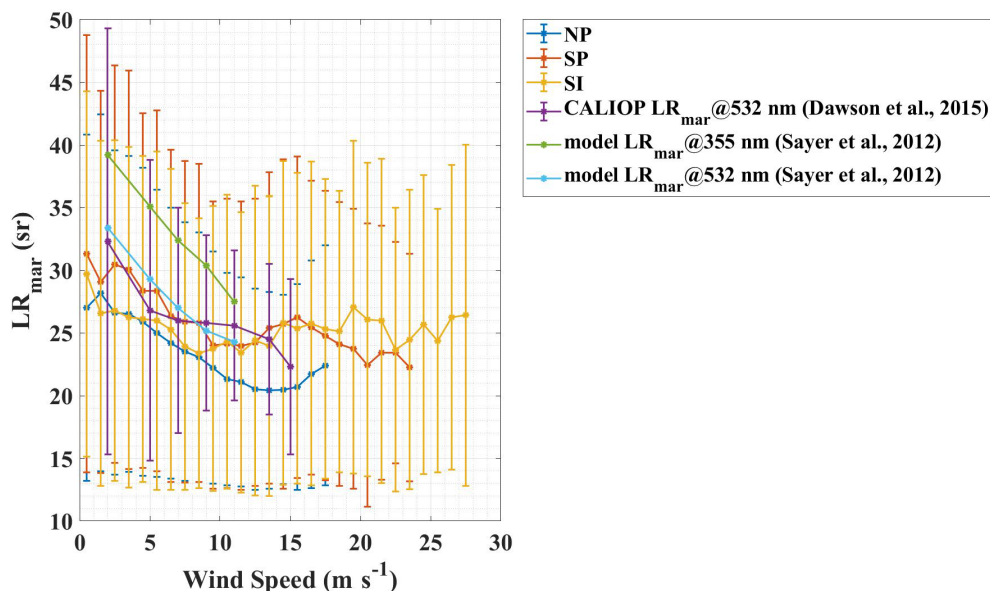
Figure 12. LR_{mar} versus wind speed. The dark blue curve, red curve, yellow curve, and the corresponding error bars represent the averaged LR_{mar} values and their standard deviations above the NP area, the SP area, and the SI area, respectively. The purple curve and the corresponding error bars represent the CALIOP-retrieved LR_{mar} at 532 nm (Dawson et al., 2015). The green curve and the light blue curve represent the modeled LR_{mar} at 355 and at 532 nm, respectively (Sayer et al., 2012).
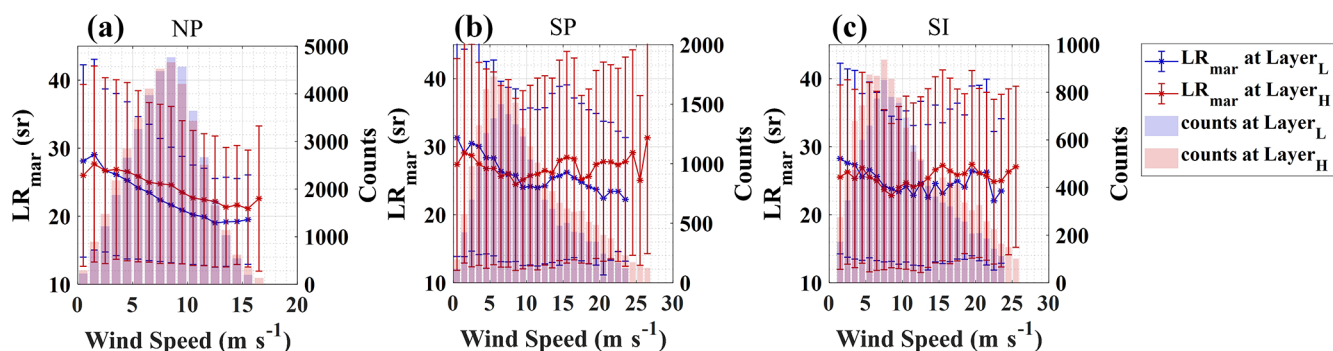
Figure 13. Averaged LR_{mar} versus wind speed, at $Layer_L$ and $Layer_H$, in **(a)** the NP area, **(b)** the SP area and **(c)** the SI area, respectively.

tribution becomes larger (Dawson et al., 2015; Smirnov et al., 2003; Sayer et al., 2012). The CALIOP LR_{mar} and the modeled LR_{mar} are all larger than the LR_{mar} of this study but are all in the standard deviation ranges. According to Groß et al. (2011, 2015), Bohlmann et al. (2018), and Floutsi et al. (2023), the pure LR_{mar} at 355 nm can vary from 10 to 40 sr, with an average of around 20 sr, and thus the averaged LR_{mar} values in this study are considered reasonable. In the medium wind speed range ($14–18\,\mathrm{m\,s^{-1}}$ of the NP area, $9–16\,\mathrm{m\,s^{-1}}$ of the SP area, and $10–20\,\mathrm{m\,s^{-1}}$ of the SI area), the LR_{mar} values show upward trends, implying that the marine aerosol particles might be broken down into smaller ones as the wind speed increases. At the very high wind speeds above the SP area ($> 16\,\mathrm{m\,s^{-1}}$) and the SI area ($> 20\,\mathrm{m\,s^{-1}}$), LR_{mar} again decreases with wind speed, which indicates that the particle

size of marine aerosol becomes larger at these wind speed conditions.

Figure 13 shows the LR_{mar} variations at $Layer_L$ and $Layer_H$ along the wind speed grid in three study areas. Some divergences in the LR_{mar} variations between the layers can be detected. As for the NP area, the variation in LR_{mar} at $Layer_L$ is from 29 sr at $1–2\,\mathrm{m\,s^{-1}}$ to 19 sr at $12–13\,\mathrm{m\,s^{-1}}$, larger than that at $Layer_H$ which is from 28 sr at $1–2\,\mathrm{m\,s^{-1}}$ to 21 sr at $15–16\,\mathrm{m\,s^{-1}}$. Regarding the SP area and the SI area, the downward trend of LR_{mar} in the high wind speed condition as mentioned above is not apparent at $Layer_H$. Moreover, at $Layer_H$, LR_{mar} can reach up to 27–28 sr at $15–25\,\mathrm{m\,s^{-1}}$, close to that at $0–5\,\mathrm{m\,s^{-1}}$, implying that the marine aerosol particle sizes at low and high wind speeds are similar.

Generally, the LR_{mar} dependence on wind speed shows a downward trend at relatively low wind speed, then an up-

ward trend at medium wind speed, and finally a downward trend again at very high wind speed (if present), which implies that the marine aerosol particle size initially increases with wind speed, then might be broken down into smaller sizes by the enhanced wind speed, and finally becomes larger again. Several differences in the LR_{mar} variations with wind speed appear between the three study areas and the two vertical layers, which may be due to the different meteorological and environmental conditions of the areas and layers.

5 Summary and conclusion

By utilizing particle optical property data (Level-2A products) and wind vector data (Level-2C products) provided by ALADIN onboard the Aeolus satellite, the correlations between marine aerosol optical properties at 355 nm and the instantaneous co-located wind speed over remote ocean areas were investigated at two separate vertical atmospheric layers (0–1 and 1–2 km, corresponding to the heights within and above the marine atmospheric boundary layer (MABL)), revealing the effect of wind speed on marine aerosol within and above the MABL over remote oceans.

Several data processing procedures were conducted to obtain pure marine aerosol data from Aeolus observations. First, three study areas located in remote oceans were selected. These areas were named the North Pacific (NP) area, the South Pacific (SP) area, and the South Indian (SI) area, respectively. The dominance of marine aerosol in these areas was then examined using the aerosol classification data provided by the VFM products of CALIOP. The proportions of marine aerosol in these areas are all larger than 79 %, while the percentage sums of marine aerosol and dusty marine aerosol are all above 90 %. Following quality control, cloud screening was performed using specific criteria (relative humidity and backscatter ratio). of the data, 9 %, 35 %, and 40 % were identified as cloud contaminated in the altitude range of 0–2 km and were subsequently eliminated for the NP area, the SP area, and the SI area, respectively. Finally, the backscatter correction was applied to the Aeolus Level-2A product. These procedures allowed us to obtain reliable, cloud-free marine aerosol optical properties and the corresponding wind speeds.

The correlations between the marine aerosol extinction coefficient (α_{mar}) and backscatter coefficient (β_{mar}) at 355 nm, as well as the wind speed, were analyzed at two separate layers for the three study areas, respectively. It was found that the Aeolus observations can provide evidence of the fact that both the layers within and above the MABL receive marine aerosol input produced and transported from the sea–air interface. Moreover, the marine aerosol load in the MABL is stronger than that at the higher layer. The enhancement of α_{mar} and β_{mar} caused by wind is more intense at the MABL. This may be due to the proximity of the MABL to the sea–air interface, making it more suscep-

tible to such effects. Furthermore, the slope variation points (15 m s^{-1} for α_{mar} and 10 m s^{-1} for β_{mar}) were found during α_{mar} and β_{mar} to increase with the wind speed. Above these slope variation points, the growth rates become lower. This phenomenon implies that the wind-driven enhancement of marine aerosol includes two phases, one of which is a rapid-growth phase with a high dependence on wind and the other is a slower-growth phase with higher fluctuations after the slope variation points. The α_{mar}–wind speed curves and the β_{mar}–wind speed curves were fitted by power-law functions and the corresponding R^2 were all higher than 0.9 for both layers and for all study areas. In addition, the relationship between AOD_{mar} at 355 nm and wind speed shows a quite consistent tendency with the regression function found in a previous study (Kiliyanpilakkil and Meskhidze, 2011) that compared CALIOP-retrieved AOD_{mar} and 10 m surface wind speed. The marine aerosol lidar ratio (LR_{mar}) and its particle size have a negative relationship. From the examination of the correlation between LR_{mar} and wind speed, it can be inferred that as the wind speed increases, the particle size of marine aerosol appears to become larger in the relatively low wind speed range, then could be broken up into smaller particles by wind at higher wind speeds, and ultimately turns out in a larger state again at very high wind speeds. As α_{mar} and β_{mar} are affected by both particle concentration and size, this reminds us that the increase in α_{mar} and β_{mar} with wind speed may not only be due to the enhancement of particulate quantity produced from the sea–air interface, but may also be impacted by the variation in size.

The regression models of α_{mar}–wind speed and β_{mar}–wind speed at two vertical layers above the three study areas are inconsistent, while the meteorological and environmental parameters, apart from the wind, differ across various regions. The production, entrainment, transport, and removal of marine aerosol above the ocean are not only dominated by the wind but also impacted by other meteorological and environmental factors, e.g., atmospheric stability, sea and air temperature, relative humidity, and others. This implies that in order to obtain more precise α_{mar} and β_{mar} models, in addition to wind speed, the abovementioned factors should be included in the establishment of the models.

This study demonstrates the ability of Aeolus to quantify interactions between aerosols and wind speeds in poorly observed ocean regions through a synergy of aerosol and wind observations based on its unique setup. The analyses of these interactions deepen our understanding of the effect of wind speed on marine aerosol optical properties over remote oceans by providing vertical information and demonstrating that their relationships are more complex than a linear or exponential relation. For the upcoming launch of EarthCARE (Earth Cloud Aerosol and Radiation Explorer) and the future planned Aeolus-2 and other vertical profile observation lidar satellites, aerosol and wind parameters with higher vertical resolution will become available. These parameters, including lidar ratios and depolarization ratios, will be helpful

for the comprehension of the relationships between marine aerosol and wind speed.

References

Abril-Gago, J., Guerrero-Rascado, J. L., Costa, M. J., Bravo-Aranda, J. A., Sicard, M., Bermejo-Pantaleón, D., Bortoli, D., Granados-Muñoz, M. J., Rodríguez-Gómez, A., Muñoz-Porcar, C., Comerón, A., Ortiz-Amezcua, P., Salgueiro, V., Jiménez-Martín, M. M., and Alados-Arboledas, L.: Statistical validation of Aeolus L2A particle backscatter coefficient retrievals over ACTRIS/EARLINET stations on the Iberian Peninsula, Atmos. Chem. Phys., 22, 1425–1451, https://doi.org/10.5194/acp-22-1425-2022, 2022.

Adames, A. F., Reynolds, M., Smirnov, A., Covert, D. S., and Ackerman, T. P.: Comparison of MODIS ocean aerosol retrievals with ship-based sun photometer measurements from the "Around the America's" expedition, J. Geophys. Res., 116, D16303, https://doi.org/10.1029/2010JD015440, 2011.

Alexander, S. P. and Protat, A.: Vertical profiling of aerosols with a combined Raman-elastic backscatter lidar in the remote Southern Ocean marine boundary layer (43–66° S, 132–150° E), J. Geophys. Res.-Atmos., 124, 12107–12125, https://doi.org/10.1029/2019JD030628, 2019.

Ansmann, A., Wandinger, U., Le Rille, O., Lajas, D., and Straume, A. G.: Particle backscatter and extinction profiling with the spaceborne high-spectral-resolution Doppler lidar ALADIN: methodology and simulations, Appl. Optics, 46, 6606, https://doi.org/10.1364/AO.46.006606, 2007.

Baars, H., Radenz, M., Floutsi, A. A., Engelmann, R., Althausen, D., Heese, B., Ansmann, A., Flament, T., Dabas, A., Trapon, D., Reitebuch, O., Bley, S., and Wandinger, U.: Californian wildfire smoke over Europe: A first example of the aerosol observing capabilities of Aeolus compared to ground-based lidar, Geophys. Res. Lett., 48, e2020GL092194, https://doi.org/10.1029/2020GL092194, 2021.

Bohlmann, S., Baars, H., Radenz, M., Engelmann, R., and Macke, A.: Ship-borne aerosol profiling with lidar over the Atlantic Ocean: from pure marine conditions to complex dust–smoke mixtures, Atmos. Chem. Phys., 18, 9661–9679, https://doi.org/10.5194/acp-18-9661-2018, 2018.

Boucher, O., Randall, D., Artaxo, P., Bretherton, C., Feingold, G., Forster, P., Kerminen, V.-M., Kondo, Y., Liao, H., Lohmann, U., Rasch, P., Satheesh, S. K., Sherwood, S., Stevens, B., and Zhang, X. Y.: Clouds and Aerosols, in: Climate Change 2013: The Physical Science Basis. Contribution of Working Group I to the Fifth Assessment Report of the Intergovernmental Panel on Climate Change, edited by: Stocker, T. F., Qin, D., Plattner, G.-K., Tignor, M., Allen, S. K., Boschung, J., Nauels, A., Xia, Y., Bex, V., and Midgley, P. M., Cambridge University Press, Cambridge, United Kingdom and New York, NY, USA, https://doi.org/10.1017/CBO9781107415324.016, 2013.

Dabas, A., Denneulin, M. L., Flamant, P., Loth, C., Garnier, A., and Dolfi-Bouteyre, A.: Correcting winds measured with a Rayleigh Doppler lidar from pressure and temperature effects, Tellus A, 60, 206–215, https://doi.org/10.1111/j.1600-0870.2007.00284.x, 2008.

Dai, G., Sun, K., Wang, X., Wu, S., E, X., Liu, Q., and Liu, B.: Dust transport and advection measurement with spaceborne lidars ALADIN and CALIOP and model reanalysis data, Atmos. Chem. Phys., 22, 7975–7993, https://doi.org/10.5194/acp-22-7975-2022, 2022.

Dawson, K. W., Meskhidze, N., Josset, D., and Gassó, S.: Space-borne observations of the lidar ratio of marine aerosols, Atmos. Chem. Phys., 15, 3241–3255, https://doi.org/10.5194/acp-15-3241-2015, 2015.

de Leeuw, G., Neele, F. P., Hill, M., Smith, M. H., and Vignati, E.: Production of sea spray aerosol in the surf zone, J. Geophys. Res., 105, 29397–29409, https://doi.org/10.1029/2000JD900549, 2000.

ESA: ESA Aeolus Online Dissemination System, https://aeolus-ds.eo.esa.int/oads/access/collection (last access: 16 February 202), 2023.

Fan, T. and Toon, O. B.: Modeling sea-salt aerosol in a coupled climate and sectional microphysical model: mass, optical depth and number concentration, Atmos. Chem. Phys., 11, 4587–4610, https://doi.org/10.5194/acp-11-4587-2011, 2011.

Flamant, P. H., Cuesta, J., Denneulin, M.-L., Dabas, A., and Huber, D.: ADM-Aeolus retrieval algorithms for aerosol and cloud products, Tellus A, 60, 273–286, https://doi.org/10.1111/j.1600-0870.2007.00287.x, 2008.

Flamant, P. H., Lever, V., Martinet, P., Flament, T., Cuesta, J., Dabas, A., Olivier, M., Huber, D., Trapon, D., and Lacour, A.: Aeolus Level-2A Algorithm Theoretical Basis Document, version 5.7, https://earth.esa.int/eogateway/documents/20142/37627/Aeolus-L2A-Algorithm-Theoretical-Baseline-Document (last access: 9 November 2022), 2020.

Flament, T., Trapon, D., Lacour, A., Dabas, A., Ehlers, F., and Huber, D.: Aeolus L2A aerosol optical properties product: standard correct algorithm and Mie correct algorithm, Atmos. Meas. Tech., 14, 7851–7871, https://doi.org/10.5194/amt-14-7851-2021, 2021.

Floutsi, A. A., Baars, H., Engelmann, R., Althausen, D., Ansmann, A., Bohlmann, S., Heese, B., Hofer, J., Kanitz, T., Haarig, M., Ohneiser, K., Radenz, M., Seifert, P., Skupin, A., Yin, Z., Abdullaev, S. F., Komppula, M., Filioglou, M., Giannakaki, E., Stachlewska, I. S., Janicka, L., Bortoli, D., Marinou, E., Amiridis, V., Gialitaki, A., Mamouri, R.-E., Barja, B., and Wandinger, U.: DeLiAn – a growing collection of depolarization ratio, lidar ratio and Ångström exponent for different aerosol types and mixtures from ground-based lidar observations, Atmos. Meas. Tech., 16, 2353–2379, https://doi.org/10.5194/amt-16-2353-2023, 2023.

Glantz, P., Nilsson, E. D., and von Hoyningen-Huene, W.: Estimating a relationship between aerosol optical thickness and surface wind speed over the ocean, Atmos. Res., 92, 58–68, https://doi.org/10.1016/j.atmosres.2008.08.010, 2009.

Grandey, B. S., Stier, P., Wagner, T. M., Grainger, R. G., and Hodges, K. I.: The effect of extratropical cyclones on satellite-retrieved aerosol properties over ocean, Geophys. Res. Lett., 38, L13805, https://doi.org/10.1029/2011GL047703, 2011.

Groß, S., Tesche, M., Freudenthaler, V., Toledano, C., Wiegner, M., Ansmann, A., Althausen, D., and Seefeldner, M.: Characterization of Saharan dust, marine aerosols and mixtures of biomass-burning aerosols and dust by means of multi-wavelength depolarization and Raman lidar measurements during SAMUM 2, Tellus B, 63, 706–724, https://doi.org/10.1111/j.1600-0889.2011.00556.x, 2011.

Groß, S., Esselborn, M., Weinzierl, B., Wirth, M., Fix, A., and Petzold, A.: Aerosol classification by airborne high spectral resolution lidar observations, Atmos. Chem. Phys., 13, 2487–2505, https://doi.org/10.5194/acp-13-2487-2013, 2013.

Groß, S., Freudenthaler, V., Wirth, M., and Weinzierl, B.: Towards an aerosol classification scheme for future EarthCARE lidar observations and implications for research needs, Atmos. Sci. Lett., 16, 77–82, https://doi.org/10.1002/asl2.524, 2015.

Haarig, M., Ansmann, A., Gasteiger, J., Kandler, K., Althausen, D., Baars, H., Radenz, M., and Farrell, D. A.: Dry versus wet marine particle optical properties: RH dependence of depolarization ratio, backscatter, and extinction from multiwavelength lidar measurements during SALTRACE, Atmos. Chem. Phys., 17, 14199–14217, https://doi.org/10.5194/acp-17-14199-2017, 2017.

Haywood, J. M., Ramaswamy, V., and Soden, B. J.: Tropospheric aerosol climate forcing in clear-sky satellite observations over the oceans, Science, 283, 1299–1303, https://doi.org/10.1126/science.283.5406.1299, 1999.

Hoaglin, D. C., Iglewicz, B., and Tukey, J. W.: Performance of some resistant rules for outlier labelling, J. Am. Stat. Assoc., 81, 991–999, https://doi.org/10.1080/01621459.1986.10478363, 1986.

Huang, H., Thomas, G. E., and Grainger, R. G.: Relationship between wind speed and aerosol optical depth over remote ocean, Atmos. Chem. Phys., 10, 5943–5950, https://doi.org/10.5194/acp-10-5943-2010, 2010.

IPCC: Summary for Policymakers, in: Climate Change 2021: The Physical Science Basis. Contribution of Working Group I to the Sixth Assessment Report of the Intergovernmental Panel on Climate Change, edited by: Masson-Delmotte, V., Zhai, P., Pirani, A., Connors, S. L., Péan, C., Berger, S., Caud, N., Chen, Y., Goldfarb, L., Gomis, M. I., Huang, M., Leitzell, K., Lonnoy, E., Matthews, J. B. R., Maycock, T. K., Waterfield, T., Yelekçi, O., Yu, R., and Zhou, B., Cambridge University Press, Cambridge, United Kingdom and New York, NY, USA, 3–32, https://doi.org/10.1017/9781009157896.001, 2021.

Jaeglé, L., Quinn, P. K., Bates, T. S., Alexander, B., and Lin, J.-T.: Global distribution of sea salt aerosols: new constraints from in situ and remote sensing observations, Atmos. Chem. Phys., 11, 3137–3157, https://doi.org/10.5194/acp-11-3137-2011, 2011.

Josset, D., Pelon, J., Protat, A., and Flamant, C.: New approach to determine aerosol optical depth from combined CALIPSO and CloudSat ocean surface echoes, Geophys. Res. Lett., 35, L10805, https://doi.org/10.1029/2008GL033442, 2008.

Kahn, R. A., Gaitley, B. J., Garay, M. J., Diner, D. J., Eck, T. F., Smirnov, A., and Holben, B. N.: Multiangle Imaging SpectroRadiometer global aerosol product assessment by comparison with the Aerosol Robotic Network, J. Geophys. Res., 115, D23209, https://doi.org/10.1029/2010JD014601, 2010.

Kanitz, T., Lochard, J., Marshall, J., McGoldrick, P., Lecrenier, O., Bravetti, P., Reitebuch, O., Rennie, M., Wernham, D., and Elfving, A.: Aeolus first light: first glimpse, International Conference on Space Optics–ICSO 2018, Chania, Greece, 9–12 October 2018, 111801R, https://doi.org/10.1117/12.2535982, 2019.

Kaufman, Y. J., Tanre, D., and Boucher, O.: A satellite view of aerosols in the climate system, Nature, 419, 215–223, https://doi.org/10.1038/nature01091, 2002.

Kiliyanpilakkil, V. P. and Meskhidze, N.: Deriving the effect of wind speed on clean marine aerosol optical properties using the A-Train satellites, Atmos. Chem. Phys., 11, 11401–11413, https://doi.org/10.5194/acp-11-11401-2011, 2011.

Kim, M.-H., Omar, A. H., Tackett, J. L., Vaughan, M. A., Winker, D. M., Trepte, C. R., Hu, Y., Liu, Z., Poole, L. R., Pitts, M. C., Kar, J., and Magill, B. E.: The CALIPSO version 4 automated

aerosol classification and lidar ratio selection algorithm, Atmos. Meas. Tech., 11, 6107–6135, https://doi.org/10.5194/amt-11-6107-2018, 2018.

Kleidman, R. G., Smirnov, A., Levy, R. C., Mattoo, S., and Tanre, D.: Evaluation and wind speed dependence of MODIS aerosol retrievals over open ocean, IEEE T. Geosci. Remote, 50, 429–435, https://doi.org/10.1109/TGRS.2011.2162073, 2012.

Labzovskii, L. D., van Zadelhoff, G. J., Tilstra, L. G., de Kloe, J., Donovan, D. P., and Stoffelen, A.: High sensitivity of Aeolus UV surface returns to surface reflectivity, Sci. Rep.-UK, 13, 17552, https://doi.org/10.1038/s41598-023-44525-5, 2023.

Latham, J. and Smith, M. H.: Effect on global warming of wind-dependent aerosol generation at the ocean surface, Nature, 347, 372–373, https://doi.org/10.1038/347372a0, 1990.

Lehahn, Y., Koren, I., Boss, E., Ben-Ami, Y., and Altaratz, O.: Estimating the maritime component of aerosol optical depth and its dependency on surface wind speed using satellite data, Atmos. Chem. Phys., 10, 6711–6720, https://doi.org/10.5194/acp-10-6711-2010, 2010.

Lewis, R. and Schwartz, E.: Sea salt aerosol production: mechanisms, methods, measurements and models – a critical review, American Geophysical Union, print ISBN 9780875904177, online ISBN 9781118666050, 2004.

Liu, Z., Kar, J., Zeng, S., Tackett, J., Vaughan, M., Avery, M., Pelon, J., Getzewich, B., Lee, K.-P., Magill, B., Omar, A., Lucker, P., Trepte, C., and Winker, D.: Discriminating between clouds and aerosols in the CALIOP version 4.1 data products, Atmos. Meas. Tech., 12, 703–734, https://doi.org/10.5194/amt-12-703-2019, 2019.

Luo, T., Yuan, R., and Wang, Z.: Lidar-based remote sensing of atmospheric boundary layer height over land and ocean, Atmos. Meas. Tech., 7, 173–182, https://doi.org/10.5194/amt-7-173-2014, 2014.

Luo, T., Wang, Z., Zhang, D., and Chen, B.: Marine boundary layer structure as observed by A-train satellites, Atmos. Chem. Phys., 16, 5891–5903, https://doi.org/10.5194/acp-16-5891-2016, 2016.

Lux, O., Lemmerz, C., Weiler, F., Marksteiner, U., Witschas, B., Rahm, S., Geiß, A., and Reitebuch, O.: Intercomparison of wind observations from the European Space Agency's Aeolus satellite mission and the ALADIN Airborne Demonstrator, Atmos. Meas. Tech., 13, 2075–2097, https://doi.org/10.5194/amt-13-2075-2020, 2020.

Madry, W. L., Toon, O. B., and O'Dowd, C. D.: Modeled optical thickness of sea salt aerosol, J. Geophys. Res., 116, D08211, https://doi.org/10.1029/2010JD014691, 2011.

Masonis, S. J., Anderson, T. L., Covert, D. S., Kapustin, V., Clarke, A. D., Howell, S., and Moore, K.: A study of the extinction-to-backscatter ratio of marine aerosol during the Shoreline Environment Aerosol Study, J. Atmos. Ocean. Tech., 20, 1388–1402, https://doi.org/10.1175/1520-0426(2003)020<1388:ASOTER>2.0.CO;2, 2003.

Meskhidze, N. and Nenes, A.: Effects of ocean ecosystem on marine aerosol-cloud interaction, Adv. Meteorol., 2010, 239808, https://doi.org/10.1155/2010/239808, 2010.

Mulcahy, J. P., O'Dowd, C. D., Jennings, S. G., and Ceburnis, D.: Significant enhancement of aerosol optical depth in marine air under wind conditions, Geophys. Res. Lett., 35, L16810, https://doi.org/10.1029/2008GL034303, 2008.

Murphy, D. M., Anderson, J. R., Quinn, P. K., Mcinnes, L. M., Brechtel, F. J., Kreidenweis, S. M., Middlebrook, A. M., Pósfai, M., Thomson, D. S., and Buseck, P. R.: Influence of sea-salt on aerosol radiative properties in the Southern Ocean marine boundary layer, Nature, 392, 62–65, https://doi.org/10.1038/32138, 1998.

NASA: Atmospheric Science Data Center, https://eosweb.larc.nasa.gov/project/CALIPSO (last access: 16 February 2023), 2023.

O'Dowd, C. D. and de Leeuw, G.: Marine aerosol production: a review of the current knowledge, Philos. T. Roy. Soc. A, 365, 1753–1774, https://doi.org/10.1098/rsta.2007.2043, 2007.

O'Dowd, C. D., Lowe, J. A., and Smith, M. H.: Coupling sea-salt and sulphate interactions and its impact on cloud droplet concentration predications, Geophys. Res. Lett., 26, 1311–1314, https://doi.org/10.1029/1999GL900231, 1999.

O'Dowd, C. D., Scannell, C., Mulcahy, J., and Jennings, S. G.: Wind speed influences on marine aerosol optical depth, Adv. Meteorol., 2010, 830846, https://doi.org/10.1155/2010/830846, 2010.

Pierce, J. R. and Adams, P. J.: Global evaluation of CCN formation by direct emission of sea salt and growth of ultrafine sea salt, J. Geophys. Res., 111, D06203, https://doi.org/10.1029/2005JD006186, 2006.

Platt, C. M. R. and Patterson, G. R.: The interpretation of baseline atmospheric turbidity measurements at Cape Grim, Tasmania, J. Atmos. Chem., 4, 187–197, https://doi.org/10.1007/BF00053778, 1986.

Prijith, S. S., Aloysius, M., and Mohan, M.: Relationship between wind speed and sea salt aerosol production: A new approach, J. Atmos. Sol.-Terr. Phy., 108, 34–40, https://doi.org/10.1016/j.jastp.2013.12.009, 2014.

Reitebuch, O.: The Spaceborne Wind Lidar Mission ADM-Aeolus, in: Atmospheric Physics, Research Topics in Aerospace, edited by: Schumann, U., Springer-Verlag Berlin Heidelberg, 815–827, ISBN 978-3-642-30182-7, https://doi.org/10.1007/978-3-642-30183-4_49, 2012.

Rennie, M., Tan, D., Andersson, E., Poli, P., Dabas, A., de Kloe, J., Marseille, G., and Stoffelen, A.: Aeolus Level-2B Algorithm Theoretical Basis Document, version 3.40, https://earth.esa.int/eogateway/documents/20142/37627/Aeolus-L2B-Algorithm-ATBD.pdf (last access: 7 November 2022), 2020.

Rennie, M. P., Isaksen, L., Weiler, F., de Kloe, J., Kanitz, T., and Reitebuch, O.: The impact of Aeolus wind retrievals on ECMWF global weather forecasts, Q. J. Roy. Meteor. Soc., 147, 3555–3586, https://doi.org/10.1002/qj.4142, 2021.

Sayer, A. M., Smirnov, A., Hsu, N. C., and Holben, B. N.: A pure marine aerosol model, for use in remote sensing applications, J. Geophys. Res., 117, D05213, https://doi.org/10.1029/2011JD016689, 2012.

Shin, D. H., Müller, D., Choi, T., Noh, Y. M., Yoon, Y. J., Lee, K. H., Shin, S. K., Chae, N., Kim, K., and Kim, Y. J.: Influence of wind speed on optical properties of aerosols in the marine boundary layer measured by ship-borne DePolarization Lidar in the coastal area of Korea, Atmos. Environ., 83, 282–290, https://doi.org/10.1016/j.atmosenv.2013.10.027, 2014.

Shinozuka, Y., Clarke, A. D., Howell, S. G., Kapustin, V. N., and Huebert, B. J.: Sea-salt vertical profiles over the Southern and tropical Pacific oceans: Microphysics, optical properties, spatial

variability, and variations with wind speed, J. Geophys. Res., 109, D24201, https://doi.org/10.1029/2004JD004975, 2004.

Smirnov, A., Villevalde, Y., O'Neill, N. T., Royer, A., and Tarussov, A.: Aerosol optical depth over the oceans: Analysis in terms of synoptic air mass types, J. Geophys. Res., 100, 16639–16650, https://doi.org/10.1029/95JD01265, 1995.

Smirnov, A., Holben, B. N., Eck, T. F., Dubovik, O., and Slutsker, I.: Effect of wind speed on columnar aerosol optical properties at Midway Island, J. Geophys. Res., 108, 4802, https://doi.org/10.1029/2003JD003879, 2003.

Smirnov, A., Sayer, A. M., Holben, B. N., Hsu, N. C., Sakerin, S. M., Macke, A., Nelson, N. B., Courcoux, Y., Smyth, T. J., Croot, P., Quinn, P. K., Sciare, J., Gulev, S. K., Piketh, S., Losno, R., Kinne, S., and Radionov, V. F.: Effect of wind speed on aerosol optical depth over remote oceans, based on data from the Maritime Aerosol Network, Atmos. Meas. Tech., 5, 377–388, https://doi.org/10.5194/amt-5-377-2012, 2012.

Stoffelen, A., Pailleux, J., Källén, E., Vaughan, J. M., Isaksen, L., Flamant, P., Wergen, W., Andersson, E., Schyberg, H., and Culoma, A.: The atmospheric dynamics mission for global wind field measurement, B. Am. Meteorol. Soc., 86, 73–88, https://doi.org/10.1175/BAMS-86-1-73, 2005.

Tan, D. G., Andersson, E., Kloe, J. D., Marseille, G.-J., Stoffelen, A., Poli, P., Denneulin, M.-L., Dabas, A., Huber, D., and Reitebuch, O.: The ADM-Aeolus wind retrieval algorithms, Tellus A, 60, 191–205, https://doi.org/10.1111/j.1600-0870.2007.00285.x, 2008.

Trapon, D., Flament, T., Lacour, A., and Stieglitz, H.: L2A user guide, issue V 2.1, https://earth.esa.int/eogateway/documents/20142/37627/Aeolus-Data-Innovation-Science-Cluster-DISC-Level-2A-user-guide.pdf (last access: 27 Feburary 2023), 2022.

Villevalde, Yu. V., Smirnov, A. V., O'Neill, N. T., Smyshlyaev, S. P., and Yakovlev, V. V.: Measurement of aerosol optical depth in the Pacific Ocean and the North Atlantic, J. Geophys. Res., 99, 20983–20988, https://doi.org/10.1029/94JD01618, 1994.

Wilson, S. R. and Forgan, B. W.: Aerosol optical depth at Cape Grim, Tasmania, 1986–1999, J. Geophys. Res., 107, D8, https://doi.org/10.1029/2001JD000398, 2002.

Winker, D. M. and Pelon, J.: The CALIPSO mission, in: IEEE International Geoscience and Remote Sensing Symposium, IGARSS'03, Proceedings, 2, 21–25 July 2003, Toulouse, France, 1329–1331, https://doi.org/10.1109/IGARSS.2003.1294098, 2003.

Winker, D. M., Vaughan, M. A., Omar, A., Hu, Y., Powell, K. A., Liu, Z., Hunt, W. H., and Young, S. A.: Overview of the CALIPSO mission and CALIOP data processing algorithms, J. Atmos. Ocean. Tech., 26, 2310–2323, https://doi.org/10.1175/2009JTECHA1281.1, 2009.

Wu, S., Sun, K., Dai, G., Wang, X., Liu, X., Liu, B., Song, X., Reitebuch, O., Li, R., Yin, J., and Wang, X.: Inter-comparison of wind measurements in the atmospheric boundary layer and the lower troposphere with Aeolus and a ground-based coherent Doppler lidar network over China, Atmos. Meas. Tech., 15, 131–148, https://doi.org/10.5194/amt-15-131-2022, 2022.

Zibordi, G., Berthon, J.-F., Melin, F., and D'Alimonte, D.: Cross-site consistent in situ measurements for satellite ocean color applications: The BiOMaP radiometric dataset, Remote Sens. Environ., 115, 2104–2115, https://doi.org/10.1016/j.rse.2011.04.013, 2011.